Published in final edited form as:

Glia. 2023 September ; 71(9): 2154–2179. doi:10.1002/glia.24385.

Microglia-specific knock-out of NF-κB/IKK2 increases accumulation of misfolded α-synuclein through inhibition of p62/SQSTM-1-dependent autophagy in the rotenone model of Parkinson's disease

Savannah M. Rocha[1,2], **Kelly S. Kirkley**[2], **Debotri Chatterjee**[3], **Tawfik A. Aboellail**[1], **Richard J. Smeyne**[3], **Ronald B. Tjalkens**[*,2]

[1]Department of Microbiology, Immunology and Pathology, Colorado State University, Fort Collins, CO 80523

[2]Department of Environmental and Radiological Health Sciences, Colorado State University, Fort Collins, CO 80523

[3]Jefferson Comprehensive Parkinson's Center, Vickie & Jack Farber Institute for Neuroscience, Thomas Jefferson University, Philadelphia, PA 19107

Abstract

Parkinson's disease (PD) is the most common neurodegenerative movement disorder worldwide, with a greater prevalence in men than women. The etiology of PD is largely unknown, although environmental exposures and neuroinflammation are linked to protein misfolding and disease progression. Activated microglia are known to promote neuroinflammation in PD, but how environmental agents interact with specific innate immune signaling pathways in microglia to stimulate conversion to a neurotoxic phenotype is not well understood. To determine how NF-κB signaling dynamics in microglia modulate neuroinflammation and dopaminergic neurodegeneration, we generated mice deficient in NF-κB activation in microglia (CX3CR1-Cre::IKK2$^{fl/fl}$) and exposed them to 2.5 mg/kg/day of rotenone for 14 days, followed by a 14-day post-lesioning incubation period. We postulated that inhibition of NF-κB signaling in microglia would reduce overall inflammatory injury in lesioned mice. Subsequent analysis indicated decreased expression of the NF-κB-regulated autophagy gene, sequestosome 1 (p62), in microglia, which is required for targeting ubiquitinated α-synuclein (α-syn) for lysosomal degradation. Knock-out animals had increased accumulation of misfolded α-syn within microglia, despite an overall reduction in neurodegeneration. Interestingly, this occurred more prominently

[*]Corresponding Author: Ronald B. Tjalkens, PhD, Department of Environmental and Radiological Health Sciences, College of Veterinary Medicine and Biomedical Sciences, Colorado State University, 1680 Campus Delivery, Physiology Building, Room 101, Fort Collins, CO 80523-1680, Tel: +1 970 491 2825, Fax: +1 970 491 7569, ron.tjalkens@colostate.edu.

Contributions

Savannah M. Rocha: conceptualization, project design, performed experimentation, data curations, algorithm formation, formal analysis, writing original draft, editing; **Kelly S. Kirkley**: performed experimentation, data curation, formal analysis, editing; **Debotri Chatterjee:** investigation, data curation, editing; **Tawfik A. Aboellail:** Investigation, data curation, editing; **Richard J. Smeyne:** investigation, data curation, editing; **Ronald B. Tjalkens:** Conceptualization, project design, investigation, data curation, editing, resources, supervision, obtained funding.

Competing Interests

The authors declare no competing interests.

in males. These data suggest that microglia play key biological roles in the degradation and clearance of misfolded α-syn and this process works in concert with the innate immune response associated with neuroinflammation. Importantly, the accumulation of misfolded α-syn protein aggregates alone did not increase neurodegeneration following exposure to rotenone but required the NF-κB-dependent inflammatory response in microglia.

Graphical Abstract

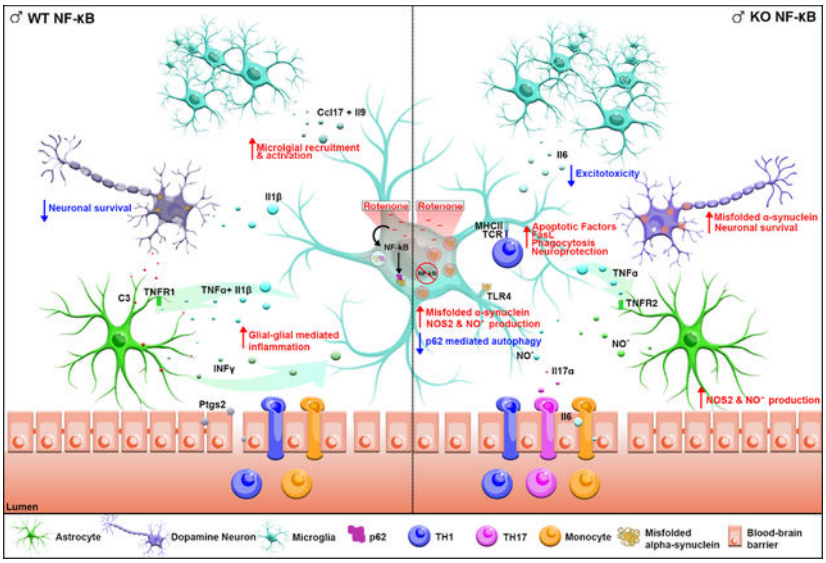

Keywords

Microglia; α-synuclein; neurodegeneration; autophagy; neuroinflammation

Introduction

Parkinson’s disease (PD) is the leading motor disorder and second most prevalent neurodegenerative disease in aging populations (Tysnes and Storstein, 2017; Marras et al., 2018). PD is characterized by progressive stages, which are clinically manifested by both non-motor and motor symptoms. In the prodromal stage of the disease, non-motor symptoms can occur decades prior to the appearance of motor symptoms and include anxiety, depression, gastrointestinal dysfunction, and anosmia (Fasano et al., 2015; Schrag and Taddei, 2017; Tarakad and Jankovic, 2017). Subsequent motor manifestations are characterized by tremor, rigidity, postural instability, masked facies, and general bradykinesia (Sveinbjornsdottir, 2016; Opara et al., 2017). Pathologically, PD is associated with a decrease in dopaminergic neurons (DAn) in the substantia nigra pars compacta (SNpc), activation of glial cells, and accumulation of misfolded α-synuclein (α-syn) protein aggregates, known as Lewy bodies, within surviving DAn soma.

Alpha-synuclein constitutes one percent of total cytosolic protein in the brain and is primarily expressed in the synaptic terminals of neurons. The physiologic function of α-syn remains largely unknown, but the regional expression of this protein increases in

the diseased state and is a major component of Lewy bodies (Spillantini et al., 1997; Wakabayashi et al., 2007; Wakabayashi et al., 2013). During neuronal stress or injury, α-syn is thought to act in a prion-like manner, whereby misfolded forms of the native protein can 'seed' the formation of additional aggregates in neighboring cells (Nonaka et al., 2010; Lashuel et al., 2013). Clearance of protein aggregates by astrocytes and microglia is important to limiting the interneuronal spread of misfolded α-syn and therefore serves as a critical modulator of the progression of PD (Scheiblich et al., 2021). Recent studies demonstrated that selective autophagy of α-syn aggregates in microglia requires interactions between sequestosome 1 (p62) interactions and ubiquinated α-syn (Choi et al., 2020). Expression of p62 is regulated by NF-κB and is therefore linked to activation of innate immune signaling pathways in microglia that respond to unfolded protein stress, such as damage and pattern recognition receptors, including the Toll-like and Nod-like receptors (Fiebich et al., 2018; Wang et al., 2020). This suggests that NF-κB may have a dual function in microglia, whereby initial activation of innate immune signaling pathways promotes clearance of α-syn protein aggregates, but chronic unfolded protein stress might trigger a reactive M1 state and the overproduction of neurotoxic inflammatory factors that further promote neuronal injury (Fernandez et al., 2021).

Microglia are specialized myeloid cells derived from the embryonic yolk sac that function as the primary innate immune cell of the central nervous system (CNS) (Masuda et al., 2022). These cells dynamically and readily respond to changes in the microenvironment of the CNS to identify and mitigate damage- and pathogen-induced stresses (Kraft et al., 2009; Kirkley et al., 2017). Upon activation, these cells undergo morphological changes from non-quiescent ramified states to ameboid, apparent through reductions in branch length, branch number, and junction number. The existence of exclusive M1 and M2 populations is highly debated, and it is now thought that there is a spectrum in which these cells dynamically adapt morphometrically in response to surrounding environmental signals (Hanisch and Kettenmann, 2007; Ransohoff, 2016; Leyh et al., 2021). Nonetheless, activated microglia are associated with prototypic inflammatory responses resulting in increased release of inflammatory cytokines and oxidative/nitrative compounds with subsequent recruitment of resident and peripheral immune cells (Jurga et al., 2020; Borst et al., 2021).

Chronic activation of microglia is implicated in the progression of many neurodegenerative diseases including multiple sclerosis, stroke, Alzheimer's Disease (AD) and PD (Gonzalez-Scarano and Baltuch, 1999; Block and Hong, 2005; Minghetti et al., 2005; Glass et al., 2010). These cells were first implicated in PD pathology in 1988, where enrichment of reactive microglia was observed in post-mortem substantia nigra (SN) samples from PD patients (McGeer et al., 1988; Badanjak et al., 2021). Nuclear factor κ B (NF-κB) inflammatory signaling pathways in microglia have been recognized as potential drivers of the inflammatory cascade where pan-inhibition of NF-κB in brain reduces α-syn spread and neurodegeneration (Dutta et al., 2021). However, it remains unknown how cell-specific inhibition of NF-κB in microglia alters morphometric, functional, and inflammatory behavior in these cells relevant to neurodegeneration and PD.

Here we used the mitochondrial complex one inhibitor, rotenone, to model the neurodegenerative and inflammatory features of PD in wildtype mice and in animals with

cell-specific deletion of IKK2/NF-κB in microglia. We demonstrate that microglia-specific knockout of NF-κB in rotenone-exposed mice have sex-dependent effects on the function of microglia, with more prominent microcytosis and chemotaxis of resident and peripheral immune cells in male animals. Reduction in activated astrocytes was also more apparent in KO male animals. NF-κB-deficient microglia had an increase of phosphorylated α-syn ($p129^+$) due to prevention of the p62-dependent autophagy pathway in male animals. Increases in $p129^+$ were also detected in DAn within the SNpc in KO mice, but despite this accumulation of $p129^+$ in microglia and DAn, overall neurodegeneration was reduced in microglia-specific NF-κB knockout males compared to wildtype controls. These results suggest that neuroinflammatory responses of microglia, rather accumulation of p129, is the primary driver of neurodegeneration in rotenone-exposed mice.

Materials and Methods

Generation of microglia-specific IKK2-NF-κB knockout animals

All animal protocols were approved by the Institutional Animal Use Committee at Colorado State University (IACUC), mice were handled in compliance with PHS Policy and Guide for the Care and Use of Laboratory Animals and procedures were performed in accordance with National Institutes of Health (NIH) guidelines. Mice were housed in microisolator cages (3–4 animals per cage), kept on a 12-h light/dark cycle and had access to both food and water *ad libitum.* Male and female heterozygous B6J.BN6(Cg)-*Cx3cr1*$^{tm1.1(cre)Jung}$/J (CX3CR1-Cre) mice were obtained from the Jackson Laboratory (Stock No. 025524, Bar Harbor ME) and bred to homozygosity. These were then paired with homozygous $IKK2^{fl/fl}$ mice (Kirkley et al., 2019) and heterozygous CX3CR1-$Cre^{+/-}$::$IKK2^{fl/fl+/-}$ littermates were crossed to obtain homozygosity for both alleles resulting in CX3CR1-$Cre^{+/+}$::$IKK2^{fl/fl\ +/+}$ (KO). $IKK2^{fl/fl\ +/+}$ were utilized at wild-type (WT) animals throughout the studies.

Isolation of primary glial cells

Mixed glial cultures from midbrain were prepared from neonatal P0-P1 WT and KO animals using previously described methods (Carbone et al., 2009; Kirkley et al., 2017). In brief, mouse pups were euthanized under isoflurane anesthesia and decapitated. Whole brain extraction from calvarium was rapidly performed and was placed in ice-cold Minimum Essential Medium with L-glutamine (MEM, Gibco/Invitrogen). Meningeal layers were gently removed from underlying brain tissue and were discarded. Tissue was completely digested with Dispase II (1.5 units/mL, ThermoFisher Scientific) and mechanical disruption. Single cell suspensions were then plated in T75 flasks with MEM media supplemented with 10% heat-inactivated fetal bovine serum (FBS) and penicillin (0.002 mg/mL), neomycin (0.001 mg/mL) and streptomycin (0.002 mg/mL) antibiotic mixture, PNS. The cells were allowed to grow to confluency under the conditions of 37°C and 5% CO_2 for ~10–14 days.

Genotyping of microglia-specific NF-κB knockout mice

Genomic DNA was extracted using Qiagen DNeasy Blood and Tissue Kits and was analyzed for concentration and purity using a Nanodrop spectrophotometer (ThermoFisher Scientific, Waltham, MA USA). Primer sets spanning a single loxP site proximal to exon3 (Forward Primer 5'-CCTTGTCCTATAGAAGCACAAC-3',

Reverse Primer 5'-GTCATTTCCACAGCCCTGTGA-3') and primer sets specific to the insertion site of Cre-recombinase in B6J.B6N(Cg)-Cx3cr1$^{tm1.1(cre)Jung}$/J (Mutant Forward Primer 5'-GACATTTGCCTTGCTGGAC-3', WT Forward Primer 5'- CCTCAGTGTGACGGAGACAG-3', and Common Cre Reverse Primer 5'-GCAGGGAAATCTGATGCAAG-3') were ordered from Integrated DNA Technologies (IDT, Coralville, IA USA). Amplicons for Cre-recombinase and LoxP insertion were generated using RT-qPCR with CYBRFast Master Mix (Tonbo) and were verified through melt curve analysis and gel electrophoresis with ethidium bromide (EtBr) staining and subsequent fluorescence imaging of both EtBr and CYBERfast Green intercalating dye. Mixed glial cultures were purified into respective astrocyte and microglial specific populations by magnetic immunoseparation as previously described (Kirkley et al., 2017) and validated through flow cytometric analysis. Microglial ionized calcium binding adaptor molecule 1 (IBA1; 1:50; Abcam, ab5076) and astrocytic glial fibrillary acidic protein (GFAP; 1:500; Abcam, ab4648) in WT and KO populations were co-stained with anti-IKK2 (1:1000; Cell Signaling, #2684) and immunofluorescence intensity analysis was performed on an Olympus VS200 (Evident, Waltham, MA USA) fully automated scanning microscope equipped with a Hamamatsu ORCA-Fusion camera (Hamamatsu Photonics, Shizuoka, Japan) and imaged with at 200X and 600X resolution using an extended apochromat X-line 20X air (0.8 N.A.) and 60X oil objective (1.42 N.A.), to obtain high magnification representative images and quantify total protein levels of IKK2 (Figure S1).

Rotenone preparation and dosing

Rotenone was prepared as previously described (Rocha et al., 2022). In brief, a 2.5 mg/kg/day dosage of 2 μL/gram body weight of rotenone was made where diluent compromised 98% medium chain-triglyceride, miglyol 812 (Cannon et al., 2009) and 2% DMSO. Male and female mice (n=9/group) were injected daily for 14 days with a dose of 2 μL/g body weight. Mice were weighed daily prior to injection to determine the appropriate dose volume. The rotenone/miglyol solution was measured using a 50 μL Hamilton syringe, which was then transferred to an insulin syringe with a fixed (29 gauge) needle and administered via intraperitoneal injection. Control animals received only miglyol injections. Hamilton syringes were cleaned every-day after use to prevent precipitation buildup within the needle. The barrel of the syringe and the plunger were submersed in 10% bleach for ten minutes, followed by aspiration of 70% ethanol then sterile water. The plunger was removed from the barrel and the syringe was allowed to air dry for 24 hours. The dosing period of 14 days was followed by a lesioning period of another 14 days. Animals were observed daily to determine morbidity or mortality.

Real-time gait analysis and open field behavioral assessment

Locomotor function by analysis of gait was investigated by recording nonrestrictive movement patterns along a one-meter fixed trackway equipped with contrasting illumination pattern allowing for pawprint visualization and pressure sensing (Hammond et al., 2018; Damale et al., 2021). Mice were acclimated to the trackway 24 hours prior to experimentation. One hour before the first dose of rotenone/miglyol, baseline (0 DPI) measurements were collected for each animal. Parameters measured included run duration, diagonal stance support for each forelimb-hind limb combination, and four-point stance

support. Data is reported as a change from 0 DPI measurement. Open field activity was measured using the Versamax behavioral system with an infrared beam grid detection array (Accuscan Instruments, Inc., Columbus, OH USA). Mice were placed within individual chambers and were monitored for five minutes under low ambient light in the presence of white noise. Animals were pre-conditioned to the chambers the day before the experimentation started. The animals were recorded one hour prior to the first dose of rotenone (0 DPI) to obtain a baseline measurement of movement. Several behavioral parameters were obtained and analyzed using Versadat Software (Accuscan Instruments, Inc., Columbus, OH USA) including change in total distance moved and the change in overall time spent moving. We have previously reported that these locomotor parameters are accurate determinants of basal ganglia function associated with decreased striatal dopamine (DA) and loss of dopaminergic innervation of the caudate/putamen (Kirkley et al., 2019; Hammond et al., 2020). Data is reported as change from 0 DPI behavioral assessment measurements.

Quantification of catecholamines and monoamines

Determination of striatal catecholamine concentrations was assessed as previously described (Hammond et al., 2020). Briefly, brain tissue was rapidly removed after decapitation under isoflurane anesthesia. Gross dissection of dorsal and ventral striatum (ST) was performed with the aid of a brain block and immediately flash frozen in liquid nitrogen, where the entire process from the time of anesthesia to flash freeze point lasted no longer than five minutes. Flash frozen striatal tissue samples were process using high-pressure liquid chromatography (HPLC) coupled with electrochemical detection to quantify the concentrations of DA, norepinephrine (NE), 3-methoxytyramine (3-MT), 3,4-dihydroxphenylacetic acid (DOPAC), homovanillic acid (HVA), serotonin (5-HT), and 5-Hydroxyindoleacetic acid (5-HIAA). Samples were analyzed using the Neurochemistry Core at Vanderbilt University's Center for Molecular Neuroscience Research (Nashville, TN USA), with randomized numerical labeling applied to all samples. All parameters obtained were normalized to overall protein concentration of each sample.

Histological evaluation and pathological scoring of brain tissue

Perfusion-fixation was performed under isoflurane anesthesia utilizing 20 mL of 0.1 M phosphate buffered-saline sodium cacodylate buffer supplemented with heparin followed by 20 mL of 4% paraformaldehyde. Brain tissue was then carefully removed and post-fixed in 10% neutral buffered formalin (NBF) for two weeks at room temperature. Each tissue specimen was then trimmed according to consistent anatomical coordinates and placed in cassettes for histological processing. Paraffin embedded brain tissue was sectioned at four and 6μm thickness and mounted to poly-ionic slides (Histotox Labs, Boulder, CO USA). Sections were deparaffinized and stained with hematoxylin and eosin on a fully automated Leica Bond RX staining robot. Each section was analyzed at 10X and 40X magnification using an Olympus IX71 microscope (Evident, Waltham, MA USA) with Retiga 2000R (Qimaging, Surrey, BC, Canada) and Qcolor3 (Evident, Waltham, MA USA) camera and Slidebook software (v6.0, Intelligent Imaging Innovations, Inc., Denver, CO USA) for image analysis. Full brain montage and high magnification images were acquired on an Olympus VS120 scanning microscope (Evident, Waltham, MA USA) equipped with a Hamamatsu

ORCA-R2 (Hamamatsu Photonics, Shizuoka, Japan) camera. Two sections per animal were analyzed by a single board certified veterinary pathologist and scored according to the following parameters: 0-unremarkable pathology; 1-more than 3–15 pyknotic neurons (up to 7 neurons) with perivascular clearing and prominent branched capillaries with mildly increased gliosis; 2-Relatively prominent gliosis on lower power magnification with multifocal clustering of apoptotic neurons and prominent vascular branching; 3-Laminar apoptosis where the affected area is greater than one 40X high power field and marked gliosis; 4-Marked neuronal apoptosis and resection from the neuropil accounting for ≥60% of the total SN with marked gliosis; 5-Marked neuronal apoptosis and resection from the neuropil accounting for ≥80% of the total SN with marked gliosis.

Automated high-throughput immunofluorescence staining of tissue sections

Paraffin embedded brain tissue was sectioned at either 4 μm or 6 μm thickness and mounted onto poly-ionic slides (Histotox Labs, Boulder, CO USA). Tissue sections were deparaffinized and immunofluorescently labeled using a Leica Bond RX_m automated robotic staining system (Leica Biosystems, Lincolnshire, IL USA). Antigen retrieval was performed by using Bond Epitope Retrieval Solution 1 for 20 minutes in conjunction with heat application. Sections were then incubated with primary antibodies diluted in 0.1% triton-X containing phosphate buffered saline (PBS): rabbit anti-tyrosine hydroxylase (TH; 1:500; Millipore, AB152), chicken anti-tyrosine hydroxylase (TH; 1:200; Abcam, ab76442), mouse anti-neuronal nuclei (NeuN; 1:200; Abcam, ab279296), mouse anti-glial fibrillary acidic protein (GFAP; 1:1000; Abcam, ab4648), rabbit anti-S100 Calcium Binding Protein B (S100β; 1:750; Abcam, ab41548), rat anti-complement component 3 (C3; 1:250; Abcam, ab11862), goat anti-ionized calcium binding adaptor molecule 1 (IBA1; 1:50; Abcam, ab5076), mouse anti-α-syn phosphorylation at serine position 129 (p129; 1:100; FUJIFILM Wako Chemicals, 015–25191), and guinea pig anti-sequestosome 1 (p62; 1:500; Progen, GP62-C). Sections were stained for DAPI (1:5000; Millipore Sigma, H3570) and mounted on glass coverslips in ProLong Gold Antifade hard set mounting medium (Fisher Scientific; P36930) and stored at 4°C until time of imaging.

Unbiased stereological analysis of neurons

Quantification of neurons was adapted from previously reported methods (Tapias and Greenamyre, 2014; Sadasivan et al., 2015; Bantle et al., 2019; Rocha et al., 2022). In brief, a 1:29 sampling fraction was used, resulting in six sections per animal being counted spanning the entire SN. Neuronal counts were conducted blindly by a single investigator. Images were captured using an automated Olympus BX63 fluorescence microscope (Evident, Waltham, MA USA) equipped with a Hamamatsu ORCA-flash 4.0 LT CCD camera (Hamamatsu Photonics, Shizuoka, Japan) and collected using Olympus CellSens software (v3.2, Evident, Waltham, MA USA). Quantitative analysis was performed on dually labeled fluorescence images generated by montage imaging of the entire coronal brain section by compiling single 100X magnification images acquired by using an Olympus X-Apochromat 10X air objective (0.40 N.A.). One hemisphere of the section was quantified by creating anatomically specific regions of interest (ROIs) based on TH immunolabeling and reference to a coronal atlas of the mouse brain (Allen Brain Atlas; Allen Institute for Brain Science; Seattle, WA USA). All images were obtained and analyzed under the same conditions

for magnification, exposure time, LED intensity, camera gain and filter settings. For quantitative assessment, TH^+ and $NeuN^+$ soma from the selected areas determined by the ROI parameters were semi-automatically counted by adaptive thresholding in the Count and Measure feature on the Olympus CellSens platform. Object filters for cellular perimeter size, minimum and maximum area, and shape factor thresholding were applied. Quantitative stereology analysis using the motorized stage method was performed as descried (Tapias and Greenamyre, 2014).

Caudal striatal sections containing dorsal ST and globus pallidus (GP) were dually or tri-stained including TH as the main marker of interest. All slides were stained and imaged simultaneously using consistent exposure times and CCD gain and binning parameters to reduce variability in intensity measurements. Whole brain montaging was performed using a 10X Olympus X-Apochromat air objective (0.04 N.A.). ROIs specific to the individualized striatal brain regions were applied and total average fluorescence intensity was determined by manual threshold masking within the CellSens platform. Representative whole brain montage images were generated using the 10X air objective and high magnification inserts were acquired using the Olympus Plan Fluorite 100X oil objective (1.30 N.A.).

Morphological and phenotypic evaluation of microglia

Morphometric analysis was performed using Imaris for neuroscientists image analysis software (v9.8.2; Bitplane Imaris; South Windsor, CT USA). Three to five randomized 400X images spanning the entirety of the substantia nigra pars reticulata (SNpr) and SNpc were taken using an Olympus X-Apochromat 40X air objective (0.95 N.A.). Filament tracing modules were used to identify $IBA1^+$ microglial processes. Somal modeling and background reduction thresholding was applied to trace and map processes associated with individual microglial cells. Total sum of processes per cell (filament length (sum)), branch number per cell (filament number of dendrite terminal points), and overall volume of processes per cell (filament volume (sum)), were utilized to determine morphometric changes present within each animal. Individual cell validation was conducted by DAPI positive nuclei co-localization with IBA1 cytoplasmic staining.

Three-dimensional renderings of glial cells were performed by using Imaris software (v9.8.2; Bitplane Imaris; South Windsor, CT USA) utilizing 100X high magnification deconvolved and mean-z projection images from 4–6 μm thickness tissue sections. Filament tracing was used to identify projection start and end points unique to individual cells based on maximal $IBA1^+$ staining intensity. Nuclei were added to renderings by spot detection determined by maximal DAPI staining intensity.

Identification and quantification of invading monocyte populations in the basal midbrain

Tissue sections were processed for immunohistochemical analysis on a fully automated Leica Bond-III RX_m (Leica Biosystems, Lincolnshire, IL USA). Epitope retrieval was performed by addition of Leica Bond Epitope Retrieval Solutions 1 and 2 for a duration of 30 minutes at 37°C. Cellular identification of monocyte lineage cell types was achieved by staining with rabbit anti-IBA1 (1:500; Abcam, ab178847) followed by 3,3'-Diaminobenzadine (DAB) chromogen. Nissl counterstain was applied for identification

of cellular nuclei. Microglia were discriminated from infiltrating peripheral macrophages by a previously established protocol that differentiates based on size and morphological differences (Smeyne et al., 2016; Bantle et al., 2021; Rocha et al., 2022). In brief, IBA1 staining outlining morphometric characteristics of each cell were scrutinized where small nuclei in combination with long thin processes denoted resting microglia, enlarged nuclei paired with shorter/thickened processes denoted activated microglia, and spherical atentril cells were peripherally invading macrophages. All quantification was performed blinded by a single investigator.

Deep learning and artificial intelligence-based quantification of glia within the substantia nigra and striatum

Two total sections per animal were selected for glial counts based on anatomical region and proximity to slides that were used to quantify DA neuron values. The studies described herein were performed blinded by a single investigator. Images utilized for quantification were captured using an automated BX63 fluorescence microscope equipped with a Hamamatsu ORCA-flash 4.0 LT CCD camera and collected using Olympus CellSens software (v3.1; Evident, Waltham, MA USA). Quantitative analysis was performed on dual or triple-labeled fluorescent images through acquisition of full brain montage scans. Each montage consisted of compiled individual 100X images taken using an Olympus X-Apochromat 10X air objective (0.4 N.A.). Dual hemispherical analysis was performed on active ROIs determined by anatomical structures identified by immunofluorescent labeling using the coronal mouse brain atlas for anatomical reference (Allen Brain Atlas; Allen Institute for Brain Science; Seattle, WA USA). All slides were imaged and scanned using the same conditions of exposure time, binning, magnification, lamp intensity and camera gain.

For identification of $GFAP^+$ cells, positive staining soma and projections within the manually drawn ROIs were detected using semi-automated cell counting software on the CellSens platform. Total area of GFAP reactivity compared to the total area sampled per animal was used to accurately quantify the amount of $GFAP^+$ astrocytes. $IBA1^+$ cell populations were identified by using deep learning artificial analysis software on the Olympus Deep Learning Platform. Optimization of neural networks was based on similarity scores ≥0.8. Manual thresholding was then applied on the probability segmentation layer to obtain total $IBA1^+$ cell counts for each specified ROI analyzed using optimized neural networks.

Fully automated deep learning neural networks were also trained to identify $S100\beta^+$ cells. This was then applied to all images across all animals within the study using batch macro-analysis to sequentially analyze up to 150 images per AI run. S100β events were then converted to ROIs and the intensity of C3 positivity was interrogated on a cell-by-cell basis for the most accurate representation of A1 reactivity within the SNpc, SNpr and ST. Manual thresholding within the Count and Measure module of CellSens was applied to batch analysis macros for mean intensity measurements of C3.

Immunohistochemical staining and quantification of protein aggregates

Sections were processed for histology and immunohistochemistry using a Leica Bond-III RX_m (Leica Biosystems, Lincolnshire, IL USA) automated staining system as described above. Reactive α-syn cell/cell aggregates were stained using mouse monoclonal anti-phosphorylated Ser129 (p129) antibody (1:100; FUJIFILM Wako Chemicals, 015–25191). Full-brain montage images were captured by using brightfield imaging on an Olympus VS120 equipped with a Hamamatsu ORCA-R2 camera. Quantification of p129 positive staining was performed by using manual HSV thresholding within the Count and Measure features of CellSens, specifically adapted for RGB files. Thresholds were kept consistent throughout all images and object filters that spanned size and signal intensity were applied. Total positive staining area and object count were plotted against overall brain region specific ROI area sampled from individual sections to obtain animal-to-animal comparisons.

Quantification of p129 protein aggregates and autophagy markers

Multi-factorial analysis was performed to determine p129 presence within two sections per animal. Overall regional intensities were measured from 10X full brain montages with the count and measure module of CellSens (v3.1; Evident, Waltham, MA USA), where manual thresholding in the channel of interest was applied to obtain mean fluorescence intensity. Five total images per section, up to 10 total per animal depending on anatomical variation, were obtained using an Olympus X-Apochromat 40X (N.A. 0.16) magnification. Cell specific gaiting parameters were applied on microglia (IBA1) and DAn (TH) where average intensity of p129 was measured per cell within each section using manual and adaptive thresholding strategies within the count and measure module of CellSens (v3.1; Evident, Waltham, MA USA). Overall intensity of p62 within $IBA1^+$ cells was performed with manual thresholding set to consistent parameters to obtain average fluorescent intensity per $IBA1^+$ event.

Detection of misfolded α-synuclein in serum via Enzyme Linked Immunosorbent Assay (ELISA)

Terminal blood samples were collected by cardiac puncture of the right atrium under deep isoflurane anesthesia. Blood was centrifuged at 845 x g for 10 minutes. Serum was then collected from the upper phase of the samples and frozen at −80°C until quantification. Serum samples were removed from the freezer and diluted 1:100 in 1X phosphate buffered saline (PBS). Protein concentration was then determined by using the Pierce BCA Protein Assay Kit (ThermoFisher Scientific, 23227). A final volume of 50 μL of 0.01 μg/μL serum, diluted in carbonate-bicarbonate buffer, was added to each well of the ELISA plate (MG Scientific, T428–12). Adhesion of the target proteins to the well surface was allowed for 1 hour at 37°C. Blocking was then performed with superblock (ThermoFisher Scientific, 37515) for 1 hour at 37°C. Primary p129 (FUJIFILM Wako Chemicals, 015–25191) was directly conjugated to horse-radish peroxidase (HRP; Abcam, ab102890) and was diluted at a 1:2,000 in 1X PBS. 100 μL of this was placed in each well and allowed to incubate at 37°C for 1 hour. Three wash steps with 0.05% PBS containing Tween 20 were performed between each antibody incubation. One-Step Ultra 3,3’,5,5’-Tetramethylbenzidine ELISA Substrate Solution (ThermoFisher Scientific, 34028) was used to develop ELISA plates for

five minutes at ambient temperature. Reactions were quenched using 0.5 M sulfuric acid. Absorbance was measured at 450 nm on a BMG LabTech POLARstar Omega microplate reader (BMG Labtech, Ortenberg, Germany) to obtain total absorbance values.

qRT-PCR array analysis

Tissue from the basal midbrain consisting primarily of SN was homogenized using a BeadBug 3 Position Head Homogenizer (Thomas Scientific, Swedesboro, NJ USA) using 2.8 mm stainless steel beads submersed in RLT buffer from the Qiagen RNeasy Mini Kit (Qiagen, Hilden, Germany). This buffer was supplemented with β-mercaptoethanol at a 1:100 dilution per sample. RNA extraction was then carried out following the Qiagen kit instructions and resulting RNA was analyzed on a Nanodrop One Spectrophotometer (ThermoFisher Scientific, Waltham, MA USA) for concentration and purity. A total of 1000 ng of RNA was used to make cDNA with iScript RT Supermix (Biorad Laboratories, 1708841). iQ SYBR Green (Biorad, 1708882) and 50ng of cDNA was subsequently loaded into each well of the QuantiNova LNA PCR Focus Panel specific for mouse inflammatory response and autoimmune gene expression profiles (Qiagen, Hilden, Germany). Relative expression ($2^{-\Delta CT}$) and fold change ($2^{-\Delta\Delta CT}$) methodology was used to determine expression changes compared to the reference genes of β-actin and β-2-microglobulin.

One step in-house arrays were also used to identify specific genes of interest associated with diseased state. RNA was isolated as previously described and was used as template in a one-step Taqman probe reaction with 1X reverse-transcriptase containing master mix and 20X RTase (Tonbo, 31–5243-0300R), 400 nM primers directed at the genes of interest, 200 nM of each probe, and 200 nM primers corresponding to the reference gene (β-*actin*). Sequences (Table S1) were validated individually and together within the same well prior to usage based on 90–110% efficiency and $R^2 \geq 0.99$. Primer and probe sequences were ordered from Integrated DNA Technologies (IDT, Coralville, IA USA) where the probe sequences synthesized were Prime Time Probes featuring individual reporter dyes with one or two quencher molecules to achieve higher signal-to-noise ratio. Delta cq and delta delta cq fold change methodology was applied to the resulting data to determine transcriptional regulation.

Gene expression profiling and analysis

Relative expression ($2^{-\Delta CT}$) and fold change ($2^{-\Delta\Delta CT}$) values were analyzed for outliers using ROUT testing, and full dataset analysis was performed on outlier excluded values using ClustVis (Metsalu and Vilo, 2015). Clade clustering was determined by cluster similarity in a correlation analysis method followed by Ward linkage. Unit variance scaling was applied and SVD with imputation settings were utilized for the generation of PCA plotting. Collapse of individual subjects into overall groups was applied for heat mapping with row centering. Fold regulation values greater than 2 (up-regulation) and less than -2 (down-regulation) were then analyzed by the programming software STRING (v.11.5; (Szklarczyk et al., 2021)) where full STRING networks were generated based on confidence with high interaction determination (0.700). Confidence was determined through textmining, experiments, databases, co-expression, neighborhood, gene fusion and co-occurrence parameters and was ultimately visualized though line thickness. Cluster

differentiation within all significantly up or down-regulated genes was calculated from k-means resulting in six possible clusters, of which were then analyzed through STRING to determine appropriate GO Term associations. Radar graph generation was performed on Python (v3.9.7; Python Software Foundation, Fredericksburg, VA USA) software with JupyterLab computational platform where fold change values were input as data points.

Statistical analysis

All data was presented as mean +/− SEM, unless otherwise noted. Experimental values from each group were analyzed with a ROUT (alpha=0.05) test to identify significant outliers and validate exclusions. Differences between three-parameter variables were determined by three-way ANOVA with subsequent Tukey *post hoc* multiple comparisons testing. Variance differences between two-parameter variables were identified using a two-way ANOVA followed by a Sidak *post hoc* multiple comparisons test. All individual variables within the same timepoint or biological sex were analyzed for variance differences using an unpaired one-way ANOVA. Significance was identified as **p<0.05, **p<0.01, ***p<0.001, ****p<0.0001.* All statistical analysis was performed using Prism (version 9.1.0; Graph Pad Software; San Diego, CA USA).

Results

Behavioral and locomotor changes are exposure, genotype, and sex dependent

To identify locomotor deficits caused by sub-acute exposure to rotenone, mice were evaluated by real-time gait analysis and open field behavioral monitoring. Real-time gait analysis of cadence and paw placement patterns of animals freely moving along a fixed trackway, revealed changes in diagonal support that varied by sex alone and the combination of rotenone exposure and genotype in male animals (Figure 1a,b,f). Differences in four-point support (Figure 1c,g) and run duration (Figure 1e,i) also varied by sex and rotenone exposure, where male WT animals exposed to rotenone had a wider base of support (Figure 1d) resulting in longer run durations (Figure 1e) to cover the same distance when compared to male animals within other genotypes and toxin exposures, or when compared to female animals. Behavioral analysis in open-field chambers was utilized to determine anxiety-like behavior and to assess additional indices of locomotor dysfunction relevant to PD throughout the course of exposure. Heat map and x,y,z plane coordinate line tracking was used to represent the overall movement of animals during five minute runs (Figure 1j–m). There was an increase in the total distance traveled in male knockout control mice relative to wild type control mice (Figure 1n), as well as a decrease in the number of rearing movements in rotenone-treated wildtype males (Figure 1p). Total movement time in male and female animals was timepoint dependent (Figure 1o,r), where only male animals displayed variance in the total time moved with respect to genotypic difference (p=0.0184, F(1,18)=6.714). Male microglial-specific IKK2 knock-out animals showed decreased movement time at 2 WPI (Figure 1o). Rearing number decreased within WT male rotenone exposed animals at 1 WPI, with no changes detected in female animals between groups at any timepoint evaluated (Figure 1p,s).

Microglia-specific knockout of NF-κB alters rotenone-induced changes in striatal neurotransmitters.

Neurochemical changes within the ST were assessed to determine relative deviations of catecholamines and monoamines in response to rotenone treatment, genotype, and sex. Quantification of catecholamines within striatal tissue revealed no significant changes in DA or 3-MT between genotype, exposure group, or sex (Figure 2a,c). DOPAC was decreased in male KO rotenone-exposed animals compared to male KO miglyol-exposed animals, where an overall effect was observed between sex, genotype and rotenone exposure (p=0.0127, F(1,47)=6.046) (Figure 2b). Levels of the DA metabolite, HVA, were decreased in rotenone-exposed KO male mice compared to rotenone-exposed WT male mice (Figure 2d). The ratio of DOPAC to DA (DOPAC/DA) was not different between groups based upon 3-way ANOVA multiple comparisons, but showed a strong trend toward an exposure effect (p=0.06, F(1,40)=3.747) (Figure 2e). Likewise, the ratio of DOPAC+HVA/DA showed no significance between any groups (Figure 2f). 5-HT levels were decreased in WT male mice between the control and rotenone-exposed groups, with a significant genotype effect (p=0.05, F(1,46)=4.011) (Figure 2g). NE was decreased in WT male mice exposed to rotenone compared to male WT controls and to KO rotenone-exposed males (Figure 2h). There were significant alterations in NE with effects detected between the following variables: sex, genotype, and exposure (p=0.0374, F(1,47)=4.589); sex and rotenone exposure (p=0.0538, F(1,47)=3.921). 5-HIAA was also decreased in male WT mice exposed to rotenone compared to WT control and to KO rotenone-exposed males (Figure 2i).

IKK2 knock-out selectively increases microcytosis in male animals

The number of microglia in the SNpc, SNpr and ST was determined in control and rotenone-exposed mice by immunofluorescence microscopy and whole-brain montage imaging for $IBA1^+$ cells (Figure 3). Representative images of immunostaining for $IBA1^+$ cells in control and rotenone-exposed WT and KO male mice are depicted for the SN (Figure 3a–d) and ST (Figure 3e–h). Changes in the morphology of microglia between exposure groups, sex, and genotype were determined using Imaris software to quantify alterations in cellular processes including branch length per cell, number of branches per cell, and the number of junctions per cell. High magnification images of microglia within the SN were converted to binary form and skeletonized in addition to generating three-dimensional rendered images along the z-axis (Figure 3 i–l). An increase in the number of microglia was observed in the SNpc and SNpr in male WT and KO mice exposed to rotenone, compared to male KO control animals. Both the SNpc and SNpr showed and effect on the number of microglia with respect to the following variable combinations: rotenone exposure and genotype; rotenone exposure and sex; and sex as a single parameter (Figure 3m,n). Multiple parameter comparisons between groups in the ST for changes in the number of microglia (Figure 3o) were not significant but there was a clear effect observed for the combination of exposure, genotype, and sex (p=0.0559, F(1,51)=3.828). Decreased maximum branch length per cell was observed in WT and KO male mice exposed to rotenone, whereas females only showed rotenone exposure differences in WT animals. Reduction in branch length was also observed in male and female KO control animals when compared to WT control animals (Figure 3p). Total branches per microglial cell revealed male only changes with reduction in WT rotenone exposed animals and KO control animals (Figure 3q). However, when comparing

genotype, there was an increase in the total number of branches in rotenone-exposed KO males compared to KO controls (Figure 3q). The total volume of individual microglial cells was reduced in male animals in the WT rotenone-exposed and KO control groups when compared to the WT control group (Figure 3r).

Differential astrocytic phenotyping and populational quantification show decreases in astrocytic activation and proliferation post-rotenone exposure in microglial IKK2 knock-out animals

The involvement of astrocytes in progressive neurodegeneration after rotenone exposure was analyzed through cellular phenotyping and regional shifts in population dynamics in the SN and ST (Figure 4). Whole brain scanning microscopy was used to evaluate the phenotype of astrocytes co-expressing GFAP, S100β, and C3 as markers for inflammatory activation. Representative montage images of male WT and KO control and rotenone exposed mice are shown for the SN (Figure 4a–d) and ST (Figure 4e–h), respectively. High magnification insets and 3D rendering from the SN depict increased GFAP immunoreactivity and C3 protein expression within $S100\beta^+$ soma and $GFAP^+$ processes in rotenone-exposed mice WT animals and KO controls (Figure 4a–d). In addition, there was substantial hypertrophy of astrocyte soma and processes in both control and rotenone-treated KO mice (Figure 4b, d). Expression of GFAP in the SNpc was selectively increased in male WT mice exposed to rotenone and in KO control animals, compared to WT control animals (Figure 4i). Interestingly, there were decreases in the expression of GFAP in male KO rotenone exposed animals compared to the KO controls. There were no significant differences between groups in female mice. Multiple group comparisons of GFAP in the SNpc revealed differences based on the following combination of variables: sex, genotype and rotenone exposure (p=0.0083, F(1,57)=7.484); genotype and rotenone exposure (p=0.0305, F(1,57)=4.925), and genotype alone (p=0.0023, F(1,57)=10.15). Within the SNpr, there were no statistically significant observations made with regards to GFAP expression (Figure 4j). Analysis of GFAP expression in the ST showed increases in $GFAP^+$ immunolabeling in male KO control animals when compared to WT controls, as well as in the KO rotenone exposure group. There was also a decrease in GFAP expression in KO rotenone exposed male animals compared to the WT rotenone exposure group. There were no statistically significant observations made within the female populations. Overall, the following combination of variables led to significant variance: sex and rotenone exposure (p=0.0008, F(1,57)=12.65); sex and genotype (p=0.0191, F(1,57)=5.823); and genotype alone (p=0.0090, F(1,57)=7.319) (Figure 4k).

The subcellular distribution of C3 in astrocytes was assessed by co-immunolabeling of C3 in astrocyte soma (S100β) and in processes (GFAP) to quantify the relative intracellular distribution of $C3^+$ puncta (Figure 4l–w). Male WT and KO animals, along with female WT animals, exposed to rotenone showed increases in process associated C3 (Figure 4l,m), whereas female KO animals exposed to rotenone had a reduction of process associated C3 (Figure 4m). Importantly, KO animals of both sexes, irrespective of exposure, had an overall reduction of C3 in astrocytic processes (Figure 4l,m). Somal C3 in the SNpc was increased in male WT animals exposed to rotenone and decreased in male KO animals exposed to rotenone (Figure 4r). There was no genotype associated difference with C3 expression in

the soma observed for female animals (Figure 4s). In contrast to C3 expression patterns observed in astrocytic processes, overall increases in somal C3 were prominent in KO control and rotenone exposed male animals (Figure 4r).

Analysis of C3 expression within the SNpr revealed increases in $GFAP^+$ processes in male WT and KO animals exposed to rotenone, consistent with what was observed within the SNpc (Figure 4n). However, female WT and KO animals exposed to rotenone had reduced levels of C3 in astrocytic processes and soma (Figure 4o,u). Male WT and KO animals exposed to rotenone also showed decreases in somal C3 expression (Figure 4t). Similar to the SNpc, KO male and female animals, irrespective of exposure, had reduced C3 expression in processes in the SNpr (Figure 4n,o). Male KO control animals and female KO rotenone-exposed animals also had reduced C3 in soma within the SNpr, whereas female KO controls had increases in somal C3 (Figure 4t,u).

Identification of astrocytic C3 cellular localization in the ST showed decreases in C3 foci within $GFAP^+$ processes in male KO and female WT animals exposed to rotenone (Figure 4p,q). Where, again, consistent with the SNpc and SNpr, there were genotypic associated reduction in overall process associated C3 within male and female animals (Figure 4p,q). C3 within astrocytic soma in the ST was decreased in male WT and KO animals and female WT rotenone exposed animals (Figure 4v,w). Akin to the process associated C3 in the SNpc, SNpr, and ST, there were genotypic reduction of somal C3 within male and female animals, irrespective of exposure, within the ST. This finding was unlike the somal C3 observed in the SNpc and SNpr (Figure 4r–w).

Inhibition of NF-κB in microglia decreases dopaminergic neurotoxicity in the SNpc

Degeneration of DAn within the SNpc and projecting fibers to the ST were analyzed in WT and KO mice exposed to rotenone by immunofluorescence imaging and quantitative stereology (Figure 5). Representative montage images and high magnification insets of male WT and KO mice in control and rotenone exposed groups are depicted for the SN (Figure 5a–d) and ST (Figure 5e–h). Morphologic features of injury are evident in neurons in both male WT and KO groups, including atrophy of neuronal perikarya and decreased intensity of TH^+ immunostaining within neuronal soma in WT rotenone exposed animals compared to WT controls (Figure 5i). These phenotypic changes in neuronal soma were also evident in male KO animals exposed to rotenone but were not significant compared to the KO control group. No changes in the number of TH^+ neurons were detected in female mice. There was a similar decrease in the total number of $NeuN^+$ neurons in male WT mice exposed to rotenone compared to control, with no changes detected in control or rotenone-treated female mice of either genotype (Figure 5j). Quantification of TH^+ immunoreactivity of dopaminergic terminals in the ST indicated decreases in male and female KO control animals when compared to WT controls (Figure 5k). Male KO rotenone exposed animals had less TH intensity when compared to WT rotenone exposed animals, but significantly more than that of male KO control animals. The overall changes between groups within the ST varied with respect to the combination of the following: genotype and rotenone exposure (p=0.0160, F(1,104)=5.993); genotype and sex (p=0.0557, F(1,104)=3.745; and genotype alone (p<0.0001, F(1,104)=32.03) (Figure 5k).

Regional analysis indicate that microglial cells function to clear misfolded α-synuclein aggregates

Immunohistochemical staining of the SN (Figure 6a–d) and ST (Figure 6e–h) show sex- and genotype dependent variance with respect to the total number of $p129^+$ immunoreactive foci in these brain regions in rotenone-treated mice. Male KO rotenone-exposed animals show more $p129^+$ objects within the SNpc, when compared to male WT mice exposed to rotenone. Inversely, female WT rotenone exposed animals had more $p129^+$ objects detected than females in the KO rotenone-exposed group in the SNpc (Figure 6i). The maximal percentage of $p129^+$ area within the SNpc was greater in male KO rotenone-exposed animals than in WT rotenone-exposed animals (Figure 6j). Ratio analysis for aggregate determination based on maximal $p129^+$ area to $p129^+$ object count, show that rotenone exposure and biological sex, independently, are drivers in the variation of aggregation of p129 observed within the SNpc (Figure 6k). There was a decrease in the number of $p129^+$ immunolabeling events in the SNpr in male WT mice exposed to rotenone compared to WT controls (Figure 6l). Female WT rotenone-exposed animals had higher $p129^+$ object counts when compared to female KO mice exposed to rotenone (Figure 6l), where genotype was a statistical driver of variance between groups (p=0.0249, F(1,73)=5.247). The total area of $p129^+$ objects within the SNpr was increased in female WT rotenone exposed tissue when compared with female KO rotenone exposed tissue. Genotype was also the driver for statistical variance in total area within the SNpr (p=0.0026, F(1,74)=9.708) (Figure 6m). Ratiometric analysis of $p129^+$ area to p129 total object count within the SNpr showed increases within male WT rotenone exposed animals when compared to control counterparts, indicating larger aggregates within this region. The same observation was present for female KO rotenone exposed animals in comparison to female KO control animals (Figure 6n). Statistical deviation within the SNpr for ratiometric determination of aggregate presence was driven by the following variable combinations: sex, genotype, and rotenone exposure (p=0.0424, F(1,57)=4.312); rotenone exposure (p=0.0064, F(1,57)=8.026).

Analysis of $p129^+$ immunostaining events in the ST revealed increases in the number of $p129^+$ object counts in male WT mice exposed to rotenone compared to WT control males. WT rotenone exposed females had decreased amounts of overall $p129^+$ objects when compared to WT control and KO rotenone exposed females (Figure 6o). The total $p129^+$ area occupied within the ST was increased in WT rotenone exposed and KO control male animals, where WT rotenone $p129^+$ area decreased in females when compared to same sex WT control. The decreases observed in the WT rotenone exposed females were significant when compared to the increases observed in the KO rotenone females (Figure 6p). Ratio analysis of $p129^+$ area to object count of $p129^+$ foci, showed no significant deviations in variance for females, however, there were significant increases in ratio values in KO control male animals when compared to WT control and KO rotenone of the same sex (Figure 6q). This indicated larger aggregate accumulation within KO control animals and smaller order accumulation of p129 in KO rotenone exposure in the ST. The combination of sex, genotype and rotenone exposure (p=0.0386, F(1,63)=4.465), sex and rotenone exposure (p=0.0007, F(1,63)=12.56, rotenone exposure alone (p=0.0030, F(1,63)=9.501, and sex

(p<0.0001, F(1,63)=47.64) were contributing factors towards the variance observed within p129$^+$ aggregation formation in the ST.

Inhibition of NF-κB in microglia leads to increased misfolded α-synuclein within dopaminergic neurons of the substantia nigra

The prevalence of misfolded α-syn in the SNpc and SNpr was determined both regionally and within individual DAn (Figure 7). High magnification images of p129 are depicted for DAn and IBA1$^+$ cells in male WT control (Figure 7a), WT rotenone-exposed (Figure 7b), KO control (Figure 7c), and KO rotenone-exposed mice (Figure 7d). The appearance of p129$^+$ puncta was noted in both IBA1$^+$ microglia and TH$^+$ neurons in WT mice exposed to rotenone (Figure 7b), as well as in KO mice in both control and rotenone-exposed groups (Figure 7c,d). Analysis of maximal regional staining intensity in the SNpc showed no significant changes in males, whereas there was a decrease in p129 immunoreactivity in the SNpc between KO control and KO rotenone-exposed females (Figure 7e). The combination of rotenone exposure, genotype and sex were all driving factors of statistical variance between groups (p=0.0387, F(1,107)=4.383) (Figure 7e). Similar sex associated trends were observed for overall immunoreactivity of p129 in the SNpr, with minimal changes detected in males, in contrast to decreased p129 staining in rotenone-exposed females for both WT and KO animals (Figure 7f). There was increased p129 intensity in TH$^+$ soma in both WT and KO males, as well as in WT and KO females exposed to rotenone (Figure 7g). Levels of p129 in serum were determined by ELISA and showed decreases in male WT mice exposed to rotenone, compared to WT control mice, as well as in KO controls compared to WT controls (Figure 7h). KO males exposed to rotenone had higher serum levels of p129 compared to KO controls. The only changes in serum levels of p129 observed in female mice was a decrease in KO rotenone-exposed mice compared to KO controls. (Figure 7h).

p62 mediated autophagy in microglia is reduced with NF-κB knock-out and leads to subsequent reduction in peripheral dissemination of p129 in males

Because p62 is an NF-κB-regulated gene that is critical for initiation of autophagy in microglia (Choi et al., 2020), we examined expression of this protein in microglia in both WT and KO mice following exposure to rotenone (Figure 8). Three-dimensional renderings of microglia within the SN were performed using Imaris software to reconstruct z-plane images, revealing differential amounts of p62 and p129 co-localizing in microglia in male mice (Figure 8a–d). Both p62$^+$ (green) and p129$^+$ (red) puncta were detected in soma and cytoplasmic processes of microglia in the SNpc. Genotype comparisons between WT and KO mice exposed to rotenone indicated a greater increase in p62$^+$ puncta in WT microglia in the SNpc than in KO microglia both in male and female mice (Figure 8e,f). Notably, baseline levels of p62 were greater in KO microglia compared to WT microglia in control male mice, a trend that was not detected in female mice. p129 intensity within WT males exposed to rotenone is significantly greater than the male WT control counter parts, which increases within the KO animals exposed to rotenone, showing an inverse relationship with the amount of p62 present within microglial cells (Figure 8g). WT females also have increased amounts of p129 within microglia when exposed to rotenone. However, KO animals show decreased amounts of p129 in microglial cells, significantly less than in WT females exposed to rotenone (Figure 8h).Principal component analysis (PCA) of p62 (Figure

8i) and p129 (Figure 8j) represent dimensionally reduced projection patterns of biological sex, rotenone exposure, and genotype where the total explained variance corresponding to principal component 1 (PC1) is 35.9% and 39.6%, and principal component 2 (PC2) is 15% and 10.2% for p62 and p129, respectively. Prediction ellipses are such that with a probability of 0.95 an observation within the same grouping will fall within the ellipse.

Transcriptional analysis of NF-κB mediated inflammatory genes reveals sex-dependent changes in expression of genes for local inflammation and immune cell recruitment

Expression of inflammatory and innate immunity gene transcription was examined using qRT-PCR arrays to analyze total RNA isolated from the basal midbrain encompassing the SN from WT and KO mice of both sexes within control and rotenone exposed groups (Figure 9). Analysis of transcript levels by heat map comparison indicated sex-dependent differences in patterns of gene expression, as well as enrichment of transcripts associated with inflammatory activation of microglia (Figure 9a). Differential expression of genes to control animals using cluster analysis was analyzed by radar plots in male and female mice of WT rotenone-exposed (Figure 9b), KO control (Figure 9c) and KO rotenone-exposed animals (Figure 9d), where cluster differentiation is as follows: Cluster 1- Regulation of toll-like receptors (TLRs) by endogenous ligand; Cluster 2 - Neutrophil and monocyte chemotaxis; Cluster 3 -TNFR2 non-canonical NF-κB pathway; Cluster 4 - Astrocyte, monocyte, and T-cell chemotaxis; Cluster 5 – Jak/Stat signaling; Cluster 6 - Complement and coagulation cascades. Male WT animals exposed to rotenone show increases in gene regulation involving the Jak/Stat pathways and TNFR2-mediated non-canonical NF-κB signaling (Figure 9b). Male control KO animals had increased expression of genes associated with regulation of TLRs and TNFR2 non-canonical NF-κB signaling, whereas female mice displayed increased levels of transcripts for neutrophil and monocyte chemotaxis (Figure 9c). Male KO rotenone-exposed animals showed enhanced differential regulation of genes for TLRs, neutrophil and monocyte chemotaxis, TNFR2 non-canonical NF-κB signaling, Jak/Stat signaling and chemotaxis of monocytes and T-cells, whereas female mice had greater upregulation of genes for complement and coagulation pathways (Figure 9d). Venn-diagram mapping of unique and shared upregulated genes in rotenone treated animals identify 9 inflammatory genes that are unique to male WT and male KO animals (Figure 9e). Male animals exposed to rotenone shared 20 upregulated genes, irrespective of genotype. STRING mapping of these and corresponding GO-terms identified enrichment of transcript levels of genes corresponding to chemotaxis, inflammatory cascades, microglial activation, and neutrophil recruitment as potential drivers of pathology (Figure 9f).

Differential gene expression indicates microglia are key drivers of peripheral immune cell recruitment and inflammation following rotenone exposure in male mice

Heat map comparison of gene expression in male (Figure 10a) and female (Figure 10d) mice revealed distinct transcriptional regulation of inflammatory genes that varied with sex, genotype, and exposure. STRING association mapping of differentially expressed genes in male and female mice are depicted for WT (Figure 10b,e) and KO (Figure 10c,f) rotenone-exposed animals, respectively. Differences in the fold-change expression of individual inflammatory genes indicated increases in *Il1β* (Figure 10g) and *Infγ* (Figure 10h) in

male WT rotenone-exposed animals, which were significant compared to WT control and KO rotenone-exposed animals. In contrast, females showed a reduction in these two genes with rotenone exposure and genotype. In addition, there were increases in transcripts for recruitment of peripheral immune cells in male KO rotenone-exposed animals. There were no significant changes observed in these genes in female animals (Figure 10i–k). The complement deposition protein, C4b, was also selectively increased in male KO controls, with no changes observed in female mice (Figure 10l).

Discussion

The contribution and importance of microglia-mediated inflammatory processes in the progressive pathology of neurodegenerative diseases has been increasingly demonstrated (Hickman et al., 2018). Activation of these cells from the resting/ramified state to the amoeboid/activated state results in stimulation of NF-κB inflammatory signaling cascades that increase production of cytokines and chemokines, leading to enhanced immune responses in parenchymal glial cells and in infiltrating lymphocytes. Selective genetic or pharmacological inhibition of NF-κB can reduce the accumulation in spread of misfolded of α-syn, as well as decrease the activation of glial cells and the loss of DAn (Bellucci et al., 2020), making this pathway an attractive target for therapeutic intervention. Despite this, it is unclear how NF-κB activation in individual glial cell subtypes contributes to the progression of PD. Here, we demonstrate for the first time, that microglia-specific knockout of NF-κB in the rotenone model of PD increases accumulation p129 in both DAn and microglial cells selectively in male mice, as well as reducing microglial clearance and dissemination of p129 into the blood. However, despite the increased cellular burden of p129, there was not an increase in neurodegeneration in the SNpc, underscoring the importance of microglial activation and autophagy as a key modulator of pathological outcomes in PD.

Altered patterns of neurobehavioral function were observed selectively in male mice in both WT and microglia-specific NF-κB KO animals following exposure to rotenone (Figure 1). Initial impairments observed in WT rotenone exposed males were not observed in females, and behavioral parameters were not different in KO females compared to those observed in WT females (Figure 1). The primary changes observed in male mice were associated with gait (Figure 1b, c, d, diagonal and four-point support) and varied with rotenone exposure, whereas the only notable group variance amongst female mice was associated with genotype (Figure 1i). Neurochemical alterations were observed in male animals for NE, HVA and the serotonin metabolites 5-HT and 5-HIAA (Figure 2). This is consistent with data from studies of PD patients, where alterations in NE and 5-HT coincide with or precede changes in DA (Espay et al., 2014; Caligiore et al., 2021). Fluctuations in noradrenergic outputs from the locus coeruleus influence early changes in dopaminergic projections to the ST (Paredes-Rodriguez et al., 2020). Notably, NE is thought to maintain DA signaling and resulting changes in NE may contribute to the progression of injury in DAn (Paredes-Rodriguez et al., 2020). Clinical data and animal models also demonstrated that alterations in serotonergic signaling significantly impact both motor and non-motor neurological manifestations of PD in non-linear progression patterns that are not consistent with observed DA loss and often occur earlier (Politis and Niccolini, 2015; Caligiore et al., 2021). This suggests an

important link between microglial signaling and bio-chemical and cellular responses that lead to early-stage neurochemical initiation of PD in males.

Microglia function as the primary innate and adaptive immune cell of the brain, providing immune surveillance and continual sampling of the CNS microenvironment (Lehnardt, 2010; Lenz and Nelson, 2018; Zengeler and Lukens, 2021). It has long been apparent that inflammation and the appearance of dystrophic, disease-associated microglia parallels aggregation of α-syn and precedes degeneration of DAn in PD (Braak et al., 1996; Ferreira and Romero-Ramos, 2018). Neuropathological examination of *post-mortem* tissue consistently reports microgliosis and microcytosis in areas of α-syn accumulation involving the SNpc irrespective of the presence or absence of cell death (Hunot et al., 1996; Knott et al., 2000; Imamura et al., 2003; Doorn et al., 2014; Ferreira and Romero-Ramos, 2018; Smajic et al., 2022). We found that increases in microglia in the SNpc, SNpr and ST were dependent upon rotenone exposure, genotype, and sex, with male KO rotenone-exposed animals displaying the highest numbers of microglia (Figure 3). Morphometric characterization of microglia is a reliable parameter for identification of reactive, intermediate and quiescent states relevant to disease, based on several cellular parameters including cellular area, branch complexity, sphericity, number of branches per cell, branch length and volume (Heindl et al., 2018; Fernandez-Arjona et al., 2019). Rotenone exposure in male animals resulted in reduction of branch length per cell and number of branches per cell, as well as the total volume of branches. Inhibition of NF-κB in females showed reduction in branch length in control animals, of which was not observed with rotenone exposure. In comparison, inhibition of NF-κB in male animals resulted in a constitutively more reactive microglial phenotype, but upon rotenone exposure in KO animals, microglia retained more branches per cell, characterized by small projections consistent with filopodia or lamellipodia (Franco-Bocanegra et al., 2019) (Figure 3). Comprehensively, these data support microglial structural remodeling aids in motility and recruitment towards chemoattractant signals that originate from rotenone induced injury, resulting in microgliosis, microcytosis, and increased pathological scoring (Figure S2). In concert, this data also importantly shows that inhibition of NF-κB does not obstruct microglial morphometric remodeling, rather the remodeling, migration, and inflammatory activation of microglial cells is a response to the crosstalk between neurons-microglia and astrocytes-microglia (Baxter et al., 2021).

Glial-glial crosstalk is a known modulator of neuroinflammation in neurodegenerative diseases. Activated microglia secrete pro-inflammatory cytokines such as IL-1α, TNF and C1qa which together are sufficient in inducing reactive phenotypic switching of astrocytes (Liddelow et al., 2017). Interestingly, knockout of NF-κB in microglia resulted in overall increases in regional GFAP immunoreactivity in male animals (Figure 4), consistent with observations that the density of $GFAP^+$ cells within the mesencephalon increases with the severity of DAn loss (Damier et al., 1993; Middeldorp and Hol, 2011). Further classification of astrocytes based on C3 expression in soma ($S100\beta^+$) indicated that astrocytes within the SNpc of male WT mice displayed a more reactive phenotype following exposure to rotenone. However, astrocytes in male KO control mice had higher basal levels of $C3^+$ puncta in soma compared to WT mice, which decreased following exposure to rotenone (Figure 4). C3 localization to the soma of female astrocytes was inverse that of males in

WT SNpc and SNpr, and process associated C3 was inverse that of males in KO SNpc, and in both genotypes within the SNpr and ST (Figure 4l–w). Ultimately, inhibition of NF-κB signaling by microglia reduced the prevalence of C3 protein in astrocytic processes ($GFAP^+$) and increased C3 in astroglia soma ($S100\beta^+$) surrounding DAn. The exact function of astrocytic C3 (intracellular or secreted) are not unequivocal, are context-dependent, and may have pro-inflammatory or neuroprotective effects (Pekna and Pekny, 2021), drawing attention to the importance of C3 cellular positioning, accumulation, and subsequent release and recognition.

Neurodegeneration of the DAn within the SNpc is a pathological hallmark of PD (Antony et al., 2013; Raza et al., 2019). Male animals exposed to rotenone experienced a significant loss of DAn within the SNpc along with trending reduction of TH intensity within the ST (Figure 5). KO male animals exposed to rotenone presented with less severe neuronal loss within the SNpc and comparable ST TH intensity loss (Figure 5i–k). TH immunolabeling is a common technique used to identify dopaminergic neurons, however other factors can alter activity of this enzyme including the aggregation of α-syn, which has been shown to alter phosphorylation of TH and subsequent DA synthesis (Bezard et al., 2003; Dunkley et al., 2004; Alerte et al., 2008; Tokuoka et al., 2011). Furthermore, gene ablation of TH in adult mice results in TH protein loss in somal bodies within the SNpc faster than the loss that is observed within the ST, comparable to the results observed within this study (Figure 2, Figure 5) (Tokuoka et al., 2011). Despite the reduction of TH^+ soma and projecting terminals, there was not an observed reduction in the levels of DA protein within the ST (Figure 2, Figure 5). Although interesting, the persistence of DA protein in parallel to overt TH loss has been previously observed and documented, where a striking 50% loss of TH protein was not sufficient enough to induce notable DA protein reduction (Kobayashi et al., 1995; Tokuoka et al., 2011). Increases in misfolded insoluble α-syn are capable of increasing DA synthesis, leading to reactive neurotoxic DA metabolites (Perez et al., 2002). This is a possible explanation for the reduction of TH^+ terminals observed within the male KO control animals due to the increase in higher order p129 (Figure 5, Figure 6). It is also known that neurodegeneration can be mediated by pathways associated with dysregulation of microglial housekeeping genes include *Trem2*, *Cxcr1* and progranulin, which act as immune checkpoints to keep microglial inflammatory responses under control and promote clearance of injurious stimuli (Hickman et al., 2018). Peripheral infiltration of immune cells along with systemic inflammation from the gut-microbiome can also alter progressive pathology, supporting that NF-κB inhibition in microglia reduce not only local inflammation that may lead to compromised blood brain barrier (BBB) integrity and selective degeneration of DAn, but also reduces invading monocyte populations through tight-junction retention and reduction of astrocyte activation (Figure 4, Figure 5, Figure 9, Figure S3).

Accumulation of misfolded α-syn in surviving DAn in the SNpc is another key neuropathological feature of PD (Antony et al., 2013; Dickson, 2018). It has remained unclear if the accumulation of this protein is a driver of pathology or if it is a result of progressive neurodegeneration. In synucleiopathies, multiple conformational strains can ‘seed’ and self-propagate further protein aggregates with numerous conformational isoforms that vary in seeding capacity based on structural integrity, size, and ability to form fibrils (Mecucci et al., 1982). Misfolded conformations that are unable to fibrilize are not capable

of inducing neurodegeneration within DAn of the SNpc (Winner et al., 2011). Analysis of immunolabeled $p129^+$ objects and total $p129^+$ area indicated that WT rotenone-exposed males had larger p129 aggregates compared to those in rotenone-exposed KO males (Figure 6). Inhibition of NF-κB in microglia in male animals resulted in decreased regional immunofluorescent intensity of p129 immunolabeling in the SN, but increased intensity within individual DAn (Figure 7). Taken together, this data show that rotenone exposure induces α-syn misfolding, potentially through specific stabilization of the amyloidogenic partially folded conformation of the protein (Breydo et al., 2012). Inflammatory mediators produced by microglial cells could also influence protein misfolding of α-syn during rotenone exposure, particularly by inducing a more oxidative microenvironment (Lashuel et al., 2013).

Impairment of the lysosomal pathway has been observed in familial and sporadic PD, enhancing the importance of the functional ability to degrade and clear misfolded proteins (Zheng and Zhang, 2021). Clearance of misfolded α-syn by microglia is dependent on p62-mediated protein autophagy that targets misfolded α-syn for ubiquitination and lysosomal fusion (Lamark et al., 2009; Choi et al., 2020). WT rotenone-exposed animals had high levels of p62 within microglial cells and inversely low levels of p129, whereas KO male animals had decreases in p62 immunoreactivity in individual microglial cells and correspondingly greater accumulation of p129 (Figure 8). This supports the role of p62-mediated autophagy in the degradation and clearance of p129 in microglia cells during rotenone-induced neurodegeneration. Misfolded p129 is a known ligand of TLR receptors, which activate MyD88-IRAK complexes leading to phosphorylation of IκBα and translocation of active NF-κB/p65 to the nucleus where it serves as a transcriptional regulator for p62 (Liu et al., 2017). Thus, deletion of *Ikk2* in microglia decreases expression of p62 and thereby impairs autophagy, leading to increased accumulation of p129 in rotenone exposed mice (Figure 8).

Increased research efforts geared toward biomarker identification in PD have focused on detection of α-syn in cerebral spinal fluid (CSF) and serum of PD patients (Gao et al., 2015; Chang et al., 2019). Analysis of p129 in serum of male mice indicated that rotenone-exposed WT mice had decreased serum p129 compared to controls, whereas KO mice had increased serum p129 compared to KO control animals (Figure 7h). In female KO mice, there was less serum p129 in rotenone-exposed animals compared to controls, whereas no differences were detected in WT female mice with respect to rotenone-exposure and serum p129 fluctuations. It is possible that the decreased levels of p129 in serum observed in rotenone-exposed animals is in part due to the specific conformation of p129 detected, where various oligomeric α-syn species can display different patterns of aggregate formation *in vivo* and *in vitro* (Lashuel et al., 2013). The extent of conformation-dependent tertiary structure of misfolded α-syn is not fully known, however, studies have shown that three PD-linked mutations in *SNCA* (A30P, E46K, and A53T) accelerate α-syn oligomerization, but only two of those (E46K and A53T) induce the ability of the protein to form fibrils (Conway et al., 1998; El-Agnaf et al., 1998; Lashuel et al., 2013). Increased total α-syn has been reported in serum of PD patients, but the various conformational subtypes have yet to be determined (Chang et al., 2019),. The data herein provides compelling evidence to suggest that the phosphorylation event at serine 129 on α-syn is not the predominant misfolded

form present in serum fractions of terminal blood. Other markers capable of identifying different conformational sites and post-translational modifications may be of better usage in the determination of circulating misfolded α-syn.

Numerous inflammatory genes are implicated in PD, including *Il6*, *Il1β*, *Tnfα*, *Nr4a2* (*Nurr1*), *Tlr2*, *Tlr6*, *Tlr4*, *Inf*, *Snca*, *Mapk*, *p62*, *Nlrp3*, and *Cxcr2* (Glass et al., 2010; Jiang et al., 2019; Giovannoni and Quintana, 2020; Pajares et al., 2020; Serdar et al., 2020; Tan et al., 2020; Li et al., 2021). Here we used qRT-PCR multiplex arrays to examine expression of a focused set of genes associated with innate immunity and inflammatory activation of microglia and astrocytes (Figures 9 and 10). These data revealed increases in genes associated with neutrophil and monocyte chemotaxis, non-canonical NF-κB signaling, astrocyte and T-cell chemotaxis and Jak/Stat signaling in male WT and KO animals exposed to rotenone, whereas KO females exposed to rotenone showed increases in genes associated with complement and coagulation cascades. There was a marked down-regulation of key inflammatory genes in KO male mice exposed to rotenone, suggesting that IKK2-dependent inflammatory signaling was critical to the observed loss of DAn. Importantly, rotenone upregulated nine distinct genes in WT mice, nine distinct genes in KO mice and 20 common genes in male WT and KO groups. The common upregulated genes segregated to groups for positive regulation of generalized chemotaxis, NF-κB signaling pathways, microglial cell activation and neutrophil chemotaxis. Distinct differences in the nine unique upregulated genes in WT males exposed to rotenone harbored *Ccl17*, *Ccl22*, *Ccr3* and *Ptgs2* (Figure 9). *Ccl17* and *Ccl22* have been implicated as potent activators of microglial cells capable of inducing ameboid morphology, whereas knock-out of *Ccl17* results in the reduction of microglial density (Fulle et al., 2018). CCR3 is found on astrocytes and when activated by Ccl26 has been shown to induce pro-inflammatory events that resulting in tissue damage and BBB impairment (Shou et al., 2019). Increases in *Ptgs2*/*Cox2* expression in the brain have been shown in both clinical PD cases along with MPTP mouse models. These finding provide evidence that increases in COX-2 contribute to the formation of the reactive dopamine-quinone intermediate, which has been implicated in idiopathic PD (Teismann et al., 2003; Minghetti, 2004).

Inhibition of microglial NF-κB in males resulted in downregulation of the pro-inflammatory genes, *Il1β* and *Infγ,* and upregulation of *Nos2*, *Fasl*, *Ccl11*, *Il6*, *Tlr4*, *Ccl4*, *Nfkb1*, *Il17a*, and *Kng1*, which are genes associated with TLR and non-canonical NF-κB signaling (Figure 9). It is known that there are dynamic interactions between neurotoxic TNFR1 and neuroprotective TNFR2 signaling pathways, where TNF-induced activation of TNFR2 signaling promotes cell survival in neurogenerative diseases (Yang et al., 2018; Orti-Casan et al., 2019). Indeed, we observed increases in TNFR2-regulated genes such as *Nfkb1*, *Nr3c1*, *Nr4a2* and *Bcl6*, in male KO rotenone animals (Fig. 9B–D, cluster 3 genes), likely a response to rotenone-induced stress. The observed increases in TNF in male KO rotenone animals, in concert with increases in TNFR2 signaling, provide evidence for microglial IKK2-mediated neuroprotection through activation of this pathway, in contrast to TNFR1 signaling associated with neurodegeneration (Figure 9, Figure 10, Figure S4). Furthermore, microglial mediated autophagy of α-syn requires TLR4 that, when activated, subsequently upregulates p62 through the NF-κB signaling pathway (Choi et al., 2020). Results observed for TLR4 transcription in $p129^{+}$ $p62^{+}$ microglia in male KO rotenone exposed animals

support a TLR4-dependent effect of p129 α-syn that is impaired in KO animals, resulting in decreased autophagy (Figure 8, Figure 9, Figure S4). FasL is constitutively expressed on astrocytes and is upregulated on activated microglial cells. The interaction of glial FasL with cells that express Fas, leads to apoptosis and elimination of effector immune cells. Collectively, it is believed that regulation through Fas-FasL glial mediated apoptosis is a critical intrinsic regulatory mechanism that controls neuroinflammation and the development of autoimmunity (Wang et al., 2013; Sonar and Lal, 2015). It is plausible that upregulation of anti-inflammatory genes, such as TNFR2 and TLRs, could be responsible for the observed reduction in rotenone driven pro-inflammatory genes, *Il1β* and *Infγ*, and the accompanying decrease in neurodegeneration in male KO animals (Figure 5, Figure 9, Figure 10, Figure S4).

Sex differences in the brain result from both short-term and long-term epigenetic affects induced by gonadal hormones (Stephen et al., 2019; Caceres et al., 2020; Davis et al., 2020). Additionally, glial cell expression of hormone receptors fluctuates with age, sex, and under pathological conditions (Liu et al., 2007; Astiz et al., 2014; Chowen and Garcia-Segura, 2021). Models of traumatic brain injury have shown that selective GPER1 agonists exert anti-inflammatory effects and reduce microglial reactivity in males and ovariectomized females, but not in females with intact ovaries (Pan et al., 2020). Male microglia are inherently more mobile than female microglia and present with more reactiveness in physiological conditions, where female microglia express more phagocytic cups and higher levels of cellular repair and inflammatory control genes. These biological sex-differences in microglial cells are likely due to hormone stimulation in pre- and post-neonatal developmental stages that permanently alter microglial transcriptional differentiation throughout adulthood (Yanguas-Casas, 2020). In support of this, sex dependent classification of transcript levels revealed rotenone induced increases in chemokine driven recruitment (*Cxcr1*, *Cxcr3*, *Cxcr2*, *Cxcl3*, *Cxcl2*, *Ccr4*, *Ccl3*) and microglial proliferation (*Csf1* and *Il7*) (Figure 10). In contrast, transcripts isolated from female rotenone exposed animals were tightly regulated regarding inflammation (Figure 10).

Collectively, these results enhance and highlight the complexity and importance of investigating biological-sex, cell-specific reactions, and behavior in the pathophysiology of neurodegeneration. Microglial knock-out of canonical NF-κB in male animals exposed to rotenone resulted in increased presence of microglia and accumulation of $p129^{+}$ α-syn in microglia and DAn of the SNpc. Despite this, there were reduced levels of C3 in astrocytes and an overall reduction in neurodegeneration, consistent with other recently published findings on microglial IKK2 impairment and resulting neurodegeneration (Wang et al., 2022). These findings effectively identify male microglial cells as key determinants of neurodegeneration in rotenone-exposed mice through primary activation of canonical NF-κB inflammatory signaling.

Supplementary Material

Refer to Web version on PubMed Central for supplementary material.

Acknowledgements

The authors would like to acknowledge Lab Animal Resources (LAR, Colorado State University) for the outstanding care and observation of the animals used in these studies. We would also like to thank Carol Dewbre and Tenley French for administrative and managerial support, along with Todd Bass and McKenzie Richards from the Colorado State University Diagnostics Laboratory for their immunohistochemical expertise. Finally, we would like to acknowledge the ultimate sacrifice given by the animals that were used to conduct these studies.

Funding Information

This work was supported by the National Institutes of Health grant number RO1ES021656-07 and RO1ES021656-08

Data Availability Statement

The data that support the findings of this study are available from the corresponding author upon reasonable request.

References

Alerte TN, Akinfolarin AA, Friedrich EE, Mader SA, Hong CS, and Perez RG (2008). Alpha-synuclein aggregation alters tyrosine hydroxylase phosphorylation and immunoreactivity: lessons from viral transduction of knockout mice. Neurosci Lett 435(1), 24–29. doi: 10.1016/j.neulet.2008.02.014. [PubMed: 18314273]

Antony PM, Diederich NJ, Kruger R, and Balling R (2013). The hallmarks of Parkinson's disease. FEBS J 280(23), 5981–5993. doi: 10.1111/febs.12335. [PubMed: 23663200]

Astiz M, Acaz-Fonseca E, and Garcia-Segura LM (2014). Sex differences and effects of estrogenic compounds on the expression of inflammatory molecules by astrocytes exposed to the insecticide dimethoate. Neurotox Res 25(3), 271–285. doi: 10.1007/s12640-013-9417-0. [PubMed: 23943137]

Badanjak K, Fixemer S, Smajic S, Skupin A, and Grunewald A (2021). The Contribution of Microglia to Neuroinflammation in Parkinson's Disease. Int J Mol Sci 22(9). doi: 10.3390/ijms22094676.

Bantle CM, Phillips AT, Smeyne RJ, Rocha SM, Olson KE, and Tjalkens RB (2019). Infection with mosquito-borne alphavirus induces selective loss of dopaminergic neurons, neuroinflammation and widespread protein aggregation. NPJ Parkinsons Dis 5, 20. doi: 10.1038/s41531-019-0090-8. [PubMed: 31531390]

Bantle CM, Rocha SM, French CT, Phillips AT, Tran K, Olson KE, et al. (2021). Astrocyte inflammatory signaling mediates alpha-synuclein aggregation and dopaminergic neuronal loss following viral encephalitis. Exp Neurol 346, 113845. doi: 10.1016/j.expneurol.2021.113845. [PubMed: 34454938]

Baxter PS, Dando O, Emelianova K, He X, McKay S, Hardingham GE, et al. (2021). Microglial identity and inflammatory responses are controlled by the combined effects of neurons and astrocytes. Cell Rep 34(12), 108882. doi: 10.1016/j.celrep.2021.108882. [PubMed: 33761343]

Bellucci A, Bubacco L, Longhena F, Parrella E, Faustini G, Porrini V, et al. (2020). Nuclear Factor-kappaB Dysregulation and alpha-Synuclein Pathology: Critical Interplay in the Pathogenesis of Parkinson's Disease. Front Aging Neurosci 12, 68. doi: 10.3389/fnagi.2020.00068. [PubMed: 32265684]

Bezard E, Gross CE, and Brotchie JM (2003). Presymptomatic compensation in Parkinson's disease is not dopamine-mediated. Trends Neurosci 26(4), 215–221. doi: 10.1016/S0166-2236(03)00038-9. [PubMed: 12689773]

Block ML, and Hong JS (2005). Microglia and inflammation-mediated neurodegeneration: multiple triggers with a common mechanism. Prog Neurobiol 76(2), 77–98. doi: 10.1016/j.pneurobio.2005.06.004. [PubMed: 16081203]

Borst K, Dumas AA, and Prinz M (2021). Microglia: Immune and non-immune functions. Immunity 54(10), 2194–2208. doi: 10.1016/j.immuni.2021.09.014. [PubMed: 34644556]

Braak H, Braak E, Yilmazer D, de Vos RA, Jansen EN, and Bohl J (1996). Pattern of brain destruction in Parkinson's and Alzheimer's diseases. J Neural Transm (Vienna) 103(4), 455–490. doi: 10.1007/BF01276421. [PubMed: 9617789]

Breydo L, Wu JW, and Uversky VN (2012). Alpha-synuclein misfolding and Parkinson's disease. Biochim Biophys Acta 1822(2), 261–285. doi: 10.1016/j.bbadis.2011.10.002. [PubMed: 22024360]

Caceres A, Jene A, Esko T, Perez-Jurado LA, and Gonzalez JR (2020). Extreme downregulation of chromosome Y and Alzheimer's disease in men. Neurobiol Aging 90, 150 e151–150 e154. doi: 10.1016/j.neurobiolaging.2020.02.003.

Caligiore D, Montedori F, Buscaglione S, and Capirchio A (2021). Increasing Serotonin to Reduce Parkinsonian Tremor. Front Syst Neurosci 15, 682990. doi: 10.3389/fnsys.2021.682990. [PubMed: 34354572]

Cannon JR, Tapias V, Na HM, Honick AS, Drolet RE, and Greenamyre JT (2009). A highly reproducible rotenone model of Parkinson's disease. Neurobiol Dis 34(2), 279–290. doi: 10.1016/j.nbd.2009.01.016. [PubMed: 19385059]

Carbone DL, Popichak KA, Moreno JA, Safe S, and Tjalkens RB (2009). Suppression of 1-methyl-4-phenyl-1,2,3,6-tetrahydropyridine-induced nitric-oxide synthase 2 expression in astrocytes by a novel diindolylmethane analog protects striatal neurons against apoptosis. Mol Pharmacol 75(1), 35–43. doi: 10.1124/mol.108.050781. [PubMed: 18840677]

Chang CW, Yang SY, Yang CC, Chang CW, and Wu YR (2019). Plasma and Serum Alpha-Synuclein as a Biomarker of Diagnosis in Patients With Parkinson's Disease. Front Neurol 10, 1388. doi: 10.3389/fneur.2019.01388. [PubMed: 32038461]

Choi I, Zhang Y, Seegobin SP, Pruvost M, Wang Q, Purtell K, et al. (2020). Microglia clear neuron-released alpha-synuclein via selective autophagy and prevent neurodegeneration. Nat Commun 11(1), 1386. doi: 10.1038/s41467-020-15119-w. [PubMed: 32170061]

Chowen JA, and Garcia-Segura LM (2021). Role of glial cells in the generation of sex differences in neurodegenerative diseases and brain aging. Mech Ageing Dev 196, 111473. doi: 10.1016/j.mad.2021.111473. [PubMed: 33766745]

Conway KA, Harper JD, and Lansbury PT (1998). Accelerated in vitro fibril formation by a mutant alpha-synuclein linked to early-onset Parkinson disease. Nat Med 4(11), 1318–1320. doi: 10.1038/3311. [PubMed: 9809558]

Damale PU, Chong EKP, Hammond SL, and Tjalkens RB (2021). A Low-Cost, Autonomous Gait Detection and Estimation System for Analyzing Gait Impairments in Mice. J Healthc Eng 2021, 9937904. doi: 10.1155/2021/9937904.

Damier P, Hirsch EC, Zhang P, Agid Y, and Javoy-Agid F (1993). Glutathione peroxidase, glial cells and Parkinson's disease. Neuroscience 52(1), 1–6. doi: 10.1016/0306-4522(93)90175-f. [PubMed: 8433802]

Davis EJ, Broestl L, Abdulai-Saiku S, Worden K, Bonham LW, Minones-Moyano E, et al. (2020). A second X chromosome contributes to resilience in a mouse model of Alzheimer's disease. Sci Transl Med 12(558). doi: 10.1126/scitranslmed.aaz5677.

Dickson DW (2018). Neuropathology of Parkinson disease. Parkinsonism Relat Disord 46 Suppl 1, S30–S33. doi: 10.1016/j.parkreldis.2017.07.033. [PubMed: 28780180]

Doorn KJ, Moors T, Drukarch B, van de Berg W, Lucassen PJ, and van Dam AM (2014). Microglial phenotypes and toll-like receptor 2 in the substantia nigra and hippocampus of incidental Lewy body disease cases and Parkinson's disease patients. Acta Neuropathol Commun 2, 90. doi: 10.1186/s40478-014-0090-1. [PubMed: 25099483]

Dunkley PR, Bobrovskaya L, Graham ME, von Nagy-Felsobuki EI, and Dickson PW (2004). Tyrosine hydroxylase phosphorylation: regulation and consequences. J Neurochem 91(5), 1025–1043. doi: 10.1111/j.1471-4159.2004.02797.x. [PubMed: 15569247]

Dutta D, Jana M, Majumder M, Mondal S, Roy A, and Pahan K (2021). Selective targeting of the TLR2/MyD88/NF-kappaB pathway reduces alpha-synuclein spreading in vitro and in vivo. Nat Commun 12(1), 5382. doi: 10.1038/s41467-021-25767-1. [PubMed: 34508096]

El-Agnaf OM, Jakes R, Curran MD, and Wallace A (1998). Effects of the mutations Ala30 to Pro and Ala53 to Thr on the physical and morphological properties of alpha-synuclein protein implicated

in Parkinson's disease. FEBS Lett 440(1–2), 67–70. doi: 10.1016/s0014-5793(98)01419-7. [PubMed: 9862427]

Espay AJ, LeWitt PA, and Kaufmann H (2014). Norepinephrine deficiency in Parkinson's disease: the case for noradrenergic enhancement. Mov Disord 29(14), 1710–1719. doi: 10.1002/mds.26048. [PubMed: 25297066]

Fasano A, Visanji NP, Liu LW, Lang AE, and Pfeiffer RF (2015). Gastrointestinal dysfunction in Parkinson's disease. Lancet Neurol 14(6), 625–639. doi: 10.1016/S1474-4422(15)00007-1. [PubMed: 25987282]

Fernandez D, Geisse A, Bernales JI, Lira A, and Osorio F (2021). The Unfolded Protein Response in Immune Cells as an Emerging Regulator of Neuroinflammation. Front Aging Neurosci 13, 682633. doi: 10.3389/fnagi.2021.682633. [PubMed: 34177557]

Fernandez-Arjona MDM, Grondona JM, Fernandez-Llebrez P, and Lopez-Avalos MD (2019). Microglial Morphometric Parameters Correlate With the Expression Level of IL-1beta, and Allow Identifying Different Activated Morphotypes. Front Cell Neurosci 13, 472. doi: 10.3389/fncel.2019.00472. [PubMed: 31708746]

Ferreira SA, and Romero-Ramos M (2018). Microglia Response During Parkinson's Disease: Alpha-Synuclein Intervention. Front Cell Neurosci 12, 247. doi: 10.3389/fncel.2018.00247. [PubMed: 30127724]

Fiebich BL, Batista CRA, Saliba SW, Yousif NM, and de Oliveira ACP (2018). Role of Microglia TLRs in Neurodegeneration. Front Cell Neurosci 12, 329. doi: 10.3389/fncel.2018.00329. [PubMed: 30333729]

Franco-Bocanegra DK, McAuley C, Nicoll JAR, and Boche D (2019). Molecular Mechanisms of Microglial Motility: Changes in Ageing and Alzheimer's Disease. Cells 8(6). doi: 10.3390/cells8060639.

Fulle L, Offermann N, Hansen JN, Breithausen B, Erazo AB, Schanz O, et al. (2018). CCL17 exerts a neuroimmune modulatory function and is expressed in hippocampal neurons. Glia 66(10), 2246–2261. doi: 10.1002/glia.23507. [PubMed: 30277599]

Gao L, Tang H, Nie K, Wang L, Zhao J, Gan R, et al. (2015). Cerebrospinal fluid alpha-synuclein as a biomarker for Parkinson's disease diagnosis: a systematic review and meta-analysis. Int J Neurosci 125(9), 645–654. doi: 10.3109/00207454.2014.961454. [PubMed: 25202803]

Giovannoni F, and Quintana FJ (2020). The Role of Astrocytes in CNS Inflammation. Trends Immunol 41(9), 805–819. doi: 10.1016/j.it.2020.07.007. [PubMed: 32800705]

Glass CK, Saijo K, Winner B, Marchetto MC, and Gage FH (2010). Mechanisms underlying inflammation in neurodegeneration. Cell 140(6), 918–934. doi: 10.1016/j.cell.2010.02.016. [PubMed: 20303880]

Gonzalez-Scarano F, and Baltuch G (1999). Microglia as mediators of inflammatory and degenerative diseases. Annu Rev Neurosci 22, 219–240. doi: 10.1146/annurev.neuro.22.1.219. [PubMed: 10202538]

Hammond SL, Bantle CM, Popichak KA, Wright KA, Thompson D, Forero C, et al. (2020). NF-kappaB Signaling in Astrocytes Modulates Brain Inflammation and Neuronal Injury Following Sequential Exposure to Manganese and MPTP During Development and Aging. Toxicol Sci 177(2), 506–520. doi: 10.1093/toxsci/kfaa115. [PubMed: 32692843]

Hammond SL, Popichak KA, Li X, Hunt LG, Richman EH, Damale PU, et al. (2018). The Nurr1 Ligand,1,1-bis(3'-Indolyl)-1-(p-Chlorophenyl)Methane, Modulates Glial Reactivity and Is Neuroprotective in MPTP-Induced Parkinsonism. J Pharmacol Exp Ther 365(3), 636–651. doi: 10.1124/jpet.117.246389. [PubMed: 29626009]

Hanisch UK, and Kettenmann H (2007). Microglia: active sensor and versatile effector cells in the normal and pathologic brain. Nat Neurosci 10(11), 1387–1394. doi: 10.1038/nn1997. [PubMed: 17965659]

Heindl S, Gesierich B, Benakis C, Llovera G, Duering M, and Liesz A (2018). Automated Morphological Analysis of Microglia After Stroke. Front Cell Neurosci 12, 106. doi: 10.3389/fncel.2018.00106. [PubMed: 29725290]

Hickman S, Izzy S, Sen P, Morsett L, and El Khoury J (2018). Microglia in neurodegeneration. Nat Neurosci 21(10), 1359–1369. doi: 10.1038/s41593-018-0242-x. [PubMed: 30258234]

Hunot S, Boissiere F, Faucheux B, Brugg B, Mouatt-Prigent A, Agid Y, et al. (1996). Nitric oxide synthase and neuronal vulnerability in Parkinson's disease. Neuroscience 72(2), 355–363. doi: 10.1016/0306-4522(95)00578-1. [PubMed: 8737406]

Imamura K, Hishikawa N, Sawada M, Nagatsu T, Yoshida M, and Hashizume Y (2003). Distribution of major histocompatibility complex class II-positive microglia and cytokine profile of Parkinson's disease brains. Acta Neuropathol 106(6), 518–526. doi: 10.1007/s00401-003-0766-2. [PubMed: 14513261]

Jiang P, Scarpa JR, Gao VD, Vitaterna MH, Kasarskis A, and Turek FW (2019). Parkinson's Disease is Associated with Dysregulations of a Dopamine-Modulated Gene Network Relevant to Sleep and Affective Neurobehaviors in the Striatum. Sci Rep 9(1), 4808. doi: 10.1038/s41598-019-41248-4. [PubMed: 30886221]

Jurga AM, Paleczna M, and Kuter KZ (2020). Overview of General and Discriminating Markers of Differential Microglia Phenotypes. Front Cell Neurosci 14, 198. doi: 10.3389/fncel.2020.00198. [PubMed: 32848611]

Kirkley KS, Popichak KA, Afzali MF, Legare ME, and Tjalkens RB (2017). Microglia amplify inflammatory activation of astrocytes in manganese neurotoxicity. J Neuroinflammation 14(1), 99. doi: 10.1186/s12974-017-0871-0. [PubMed: 28476157]

Kirkley KS, Popichak KA, Hammond SL, Davies C, Hunt L, and Tjalkens RB (2019). Genetic suppression of IKK2/NF-kappaB in astrocytes inhibits neuroinflammation and reduces neuronal loss in the MPTP-Probenecid model of Parkinson's disease. Neurobiol Dis 127, 193–209. doi: 10.1016/j.nbd.2019.02.020. [PubMed: 30818064]

Knott C, Stern G, and Wilkin GP (2000). Inflammatory regulators in Parkinson's disease: iNOS, lipocortin-1, and cyclooxygenases-1 and -2. Mol Cell Neurosci 16(6), 724–739. doi: 10.1006/mcne.2000.0914. [PubMed: 11124893]

Kobayashi K, Morita S, Sawada H, Mizuguchi T, Yamada K, Nagatsu I, et al. (1995). Targeted disruption of the tyrosine hydroxylase locus results in severe catecholamine depletion and perinatal lethality in mice. J Biol Chem 270(45), 27235–27243. doi: 10.1074/jbc.270.45.27235. [PubMed: 7592982]

Kraft AD, McPherson CA, and Harry GJ (2009). Heterogeneity of microglia and TNF signaling as determinants for neuronal death or survival. Neurotoxicology 30(5), 785–793. doi: 10.1016/j.neuro.2009.07.001. [PubMed: 19596372]

Lamark T, Kirkin V, Dikic I, and Johansen T (2009). NBR1 and p62 as cargo receptors for selective autophagy of ubiquitinated targets. Cell Cycle 8(13), 1986–1990. doi: 10.4161/cc.8.13.8892. [PubMed: 19502794]

Lashuel HA, Overk CR, Oueslati A, and Masliah E (2013). The many faces of alpha-synuclein: from structure and toxicity to therapeutic target. Nat Rev Neurosci 14(1), 38–48. doi: 10.1038/nrn3406. [PubMed: 23254192]

Lehnardt S (2010). Innate immunity and neuroinflammation in the CNS: the role of microglia in Toll-like receptor-mediated neuronal injury. Glia 58(3), 253–263. doi: 10.1002/glia.20928. [PubMed: 19705460]

Lenz KM, and Nelson LH (2018). Microglia and Beyond: Innate Immune Cells As Regulators of Brain Development and Behavioral Function. Front Immunol 9, 698. doi: 10.3389/fimmu.2018.00698. [PubMed: 29706957]

Leyh J, Paeschke S, Mages B, Michalski D, Nowicki M, Bechmann I, et al. (2021). Classification of Microglial Morphological Phenotypes Using Machine Learning. Front Cell Neurosci 15, 701673. doi: 10.3389/fncel.2021.701673. [PubMed: 34267628]

Li Y, Xia Y, Yin S, Wan F, Hu J, Kou L, et al. (2021). Targeting Microglial alpha-Synuclein/TLRs/NF-kappaB/NLRP3 Inflammasome Axis in Parkinson's Disease. Front Immunol 12, 719807. doi: 10.3389/fimmu.2021.719807. [PubMed: 34691027]

Liddelow SA, Guttenplan KA, Clarke LE, Bennett FC, Bohlen CJ, Schirmer L, et al. (2017). Neurotoxic reactive astrocytes are induced by activated microglia. Nature 541(7638), 481–487. doi: 10.1038/nature21029. [PubMed: 28099414]

Liu M, Hurn PD, Roselli CE, and Alkayed NJ (2007). Role of P450 aromatase in sex-specific astrocytic cell death. J Cereb Blood Flow Metab 27(1), 135–141. doi: 10.1038/sj.jcbfm.9600331. [PubMed: 16736049]

Liu T, Zhang L, Joo D, and Sun SC (2017). NF-kappaB signaling in inflammation. Signal Transduct Target Ther 2. doi: 10.1038/sigtrans.2017.23.

Marras C, Beck JC, Bower JH, Roberts E, Ritz B, Ross GW, et al. (2018). Prevalence of Parkinson's disease across North America. NPJ Parkinsons Dis 4, 21. doi: 10.1038/s41531-018-0058-0. [PubMed: 30003140]

Masuda T, Amann L, Monaco G, Sankowski R, Staszewski O, Krueger M, et al. (2022). Specification of CNS macrophage subsets occurs postnatally in defined niches. Nature 604(7907), 740–748. doi: 10.1038/s41586-022-04596-2. [PubMed: 35444273]

McGeer PL, Itagaki S, Boyes BE, and McGeer EG (1988). Reactive microglia are positive for HLA-DR in the substantia nigra of Parkinson's and Alzheimer's disease brains. Neurology 38(8), 1285–1291. doi: 10.1212/wnl.38.8.1285. [PubMed: 3399080]

Mecucci C, Donti E, Bocchini V, Tabilio A, and Martelli MF (1982). 5q-Syndrome in a patient with chronic exposure to ionizing radiation. Cancer Genet Cytogenet 5(1), 75–80. doi: 10.1016/0165-4608(82)90042-5. [PubMed: 7066875]

Metsalu T, and Vilo J (2015). ClustVis: a web tool for visualizing clustering of multivariate data using Principal Component Analysis and heatmap. Nucleic Acids Res 43(W1), W566–570. doi: 10.1093/nar/gkv468. [PubMed: 25969447]

Middeldorp J, and Hol EM (2011). GFAP in health and disease. Prog Neurobiol 93(3), 421–443. doi: 10.1016/j.pneurobio.2011.01.005. [PubMed: 21219963]

Minghetti L (2004). Cyclooxygenase-2 (COX-2) in inflammatory and degenerative brain diseases. J Neuropathol Exp Neurol 63(9), 901–910. doi: 10.1093/jnen/63.9.901. [PubMed: 15453089]

Minghetti L, Ajmone-Cat MA, De Berardinis MA, and De Simone R (2005). Microglial activation in chronic neurodegenerative diseases: roles of apoptotic neurons and chronic stimulation. Brain Res Brain Res Rev 48(2), 251–256. doi: 10.1016/j.brainresrev.2004.12.015. [PubMed: 15850664]

Nonaka T, Watanabe ST, Iwatsubo T, and Hasegawa M (2010). Seeded aggregation and toxicity of {alpha}-synuclein and tau: cellular models of neurodegenerative diseases. J Biol Chem 285(45), 34885–34898. doi: 10.1074/jbc.M110.148460. [PubMed: 20805224]

Opara J, Malecki A, Malecka E, and Socha T (2017). Motor assessment in Parkinson`s disease. Ann Agric Environ Med 24(3), 411–415. doi: 10.5604/12321966.1232774. [PubMed: 28954481]

Orti-Casan N, Wu Y, Naude PJW, De Deyn PP, Zuhorn IS, and Eisel ULM (2019). Targeting TNFR2 as a Novel Therapeutic Strategy for Alzheimer's Disease. Front Neurosci 13, 49. doi: 10.3389/fnins.2019.00049. [PubMed: 30778285]

Pajares M, A IR, Manda G, Bosca L, and Cuadrado A (2020). Inflammation in Parkinson's Disease: Mechanisms and Therapeutic Implications. Cells 9(7). doi: 10.3390/cells9071687.

Pan MX, Li J, Ma C, Fu K, Li ZQ, and Wang ZF (2020). Sex-dependent effects of GPER activation on neuroinflammation in a rat model of traumatic brain injury. Brain Behav Immun 88, 421–431. doi: 10.1016/j.bbi.2020.04.005. [PubMed: 32272225]

Paredes-Rodriguez E, Vegas-Suarez S, Morera-Herreras T, De Deurwaerdere P, and Miguelez C (2020). The Noradrenergic System in Parkinson's Disease. Front Pharmacol 11, 435. doi: 10.3389/fphar.2020.00435. [PubMed: 32322208]

Pekna M, and Pekny M (2021). The Complement System: A Powerful Modulator and Effector of Astrocyte Function in the Healthy and Diseased Central Nervous System. Cells 10(7). doi: 10.3390/cells10071812.

Perez RG, Waymire JC, Lin E, Liu JJ, Guo F, and Zigmond MJ (2002). A role for alpha-synuclein in the regulation of dopamine biosynthesis. J Neurosci 22(8), 3090–3099. doi: 20026307. [PubMed: 11943812]

Politis M, and Niccolini F (2015). Serotonin in Parkinson's disease. Behav Brain Res 277, 136–145. doi: 10.1016/j.bbr.2014.07.037. [PubMed: 25086269]

Ransohoff RM (2016). A polarizing question: do M1 and M2 microglia exist? Nat Neurosci 19(8), 987–991. doi: 10.1038/nn.4338. [PubMed: 27459405]

Raza C, Anjum R, and Shakeel NUA (2019). Parkinson's disease: Mechanisms, translational models and management strategies. Life Sci 226, 77–90. doi: 10.1016/j.lfs.2019.03.057. [PubMed: 30980848]

Rocha SM, Bantle CM, Aboellail T, Chatterjee D, Smeyne RJ, and Tjalkens RB (2022). Rotenone induces regionally distinct alpha-synuclein protein aggregation and activation of glia prior to loss of dopaminergic neurons in C57Bl/6 mice. Neurobiol Dis 167, 105685. doi: 10.1016/j.nbd.2022.105685. [PubMed: 35257879]

Sadasivan S, Zanin M, O'Brien K, Schultz-Cherry S, and Smeyne RJ (2015). Induction of microglia activation after infection with the non-neurotropic A/CA/04/2009 H1N1 influenza virus. PLoS One 10(4), e0124047. doi: 10.1371/journal.pone.0124047. [PubMed: 25861024]

Scheiblich H, Dansokho C, Mercan D, Schmidt SV, Bousset L, Wischhof L, et al. (2021). Microglia jointly degrade fibrillar alpha-synuclein cargo by distribution through tunneling nanotubes. Cell 184(20), 5089–5106 e5021. doi: 10.1016/j.cell.2021.09.007. [PubMed: 34555357]

Schrag A, and Taddei RN (2017). Depression and Anxiety in Parkinson's Disease. Int Rev Neurobiol 133, 623–655. doi: 10.1016/bs.irn.2017.05.024. [PubMed: 28802935]

Serdar M, Kempe K, Herrmann R, Picard D, Remke M, Herz J, et al. (2020). Involvement of CXCL1/CXCR2 During Microglia Activation Following Inflammation-Sensitized Hypoxic-Ischemic Brain Injury in Neonatal Rats. Front Neurol 11, 540878. doi: 10.3389/fneur.2020.540878. [PubMed: 33123073]

Shou J, Peng J, Zhao Z, Huang X, Li H, Li L, et al. (2019). CCL26 and CCR3 are associated with the acute inflammatory response in the CNS in experimental autoimmune encephalomyelitis. J Neuroimmunol 333, 576967. doi: 10.1016/j.jneuroim.2019.576967. [PubMed: 31151084]

Smajic S, Prada-Medina CA, Landoulsi Z, Ghelfi J, Delcambre S, Dietrich C, et al. (2022). Single-cell sequencing of human midbrain reveals glial activation and a Parkinson-specific neuronal state. Brain 145(3), 964–978. doi: 10.1093/brain/awab446. [PubMed: 34919646]

Smeyne RJ, Breckenridge CB, Beck M, Jiao Y, Butt MT, Wolf JC, et al. (2016). Assessment of the Effects of MPTP and Paraquat on Dopaminergic Neurons and Microglia in the Substantia Nigra Pars Compacta of C57BL/6 Mice. PLoS One 11(10), e0164094. doi: 10.1371/journal.pone.0164094. [PubMed: 27788145]

Sonar S, and Lal G (2015). Role of Tumor Necrosis Factor Superfamily in Neuroinflammation and Autoimmunity. Front Immunol 6, 364. doi: 10.3389/fimmu.2015.00364. [PubMed: 26257732]

Spillantini MG, Schmidt ML, Lee VM, Trojanowski JQ, Jakes R, and Goedert M (1997). Alpha-synuclein in Lewy bodies. Nature 388(6645), 839–840. doi: 10.1038/42166. [PubMed: 9278044]

Stephen TL, Cacciottolo M, Balu D, Morgan TE, LaDu MJ, Finch CE, et al. (2019). APOE genotype and sex affect microglial interactions with plaques in Alzheimer's disease mice. Acta Neuropathol Commun 7(1), 82. doi: 10.1186/s40478-019-0729-z. [PubMed: 31113487]

Sveinbjornsdottir S (2016). The clinical symptoms of Parkinson's disease. J Neurochem 139 Suppl 1, 318–324. doi: 10.1111/jnc.13691. [PubMed: 27401947]

Szklarczyk D, Gable AL, Nastou KC, Lyon D, Kirsch R, Pyysalo S, et al. (2021). The STRING database in 2021: customizable protein-protein networks, and functional characterization of user-uploaded gene/measurement sets. Nucleic Acids Res 49(D1), D605–D612. doi: 10.1093/nar/gkaa1074. [PubMed: 33237311]

Tan JSY, Chao YX, Rotzschke O, and Tan EK (2020). New Insights into Immune-Mediated Mechanisms in Parkinson's Disease. Int J Mol Sci 21(23). doi: 10.3390/ijms21239302.

Tapias V, and Greenamyre JT (2014). A rapid and sensitive automated image-based approach for in vitro and in vivo characterization of cell morphology and quantification of cell number and neurite architecture. Curr Protoc Cytom 68, 12 33 11–22. doi: 10.1002/0471142956.cy1233s68.

Tarakad A, and Jankovic J (2017). Anosmia and Ageusia in Parkinson's Disease. Int Rev Neurobiol 133, 541–556. doi: 10.1016/bs.irn.2017.05.028. [PubMed: 28802932]

Teismann P, Tieu K, Choi DK, Wu DC, Naini A, Hunot S, et al. (2003). Cyclooxygenase-2 is instrumental in Parkinson's disease neurodegeneration. Proc Natl Acad Sci U S A 100(9), 5473–5478. doi: 10.1073/pnas.0837397100. [PubMed: 12702778]

Tokuoka H, Muramatsu S, Sumi-Ichinose C, Sakane H, Kojima M, Aso Y, et al. (2011). Compensatory regulation of dopamine after ablation of the tyrosine hydroxylase gene in the nigrostriatal

projection. J Biol Chem 286(50), 43549–43558. doi: 10.1074/jbc.M111.284729. [PubMed: 22027820]

Tysnes OB, and Storstein A (2017). Epidemiology of Parkinson's disease. J Neural Transm (Vienna) 124(8), 901–905. doi: 10.1007/s00702-017-1686-y. [PubMed: 28150045]

Wakabayashi K, Tanji K, Mori F, and Takahashi H (2007). The Lewy body in Parkinson's disease: molecules implicated in the formation and degradation of alpha-synuclein aggregates. Neuropathology 27(5), 494–506. doi: 10.1111/j.1440-1789.2007.00803.x. [PubMed: 18018486]

Wakabayashi K, Tanji K, Odagiri S, Miki Y, Mori F, and Takahashi H (2013). The Lewy body in Parkinson's disease and related neurodegenerative disorders. Mol Neurobiol 47(2), 495–508. doi: 10.1007/s12035-012-8280-y. [PubMed: 22622968]

Wang C, Fan L, Khawaja RR, Liu B, Zhan L, Kodama L, et al. (2022). Microglial NF-kappaB drives tau spreading and toxicity in a mouse model of tauopathy. Nat Commun 13(1), 1969. doi: 10.1038/s41467-022-29552-6. [PubMed: 35413950]

Wang M, Ye X, Hu J, Zhao Q, Lv B, Ma W, et al. (2020). NOD1/RIP2 signalling enhances the microglia-driven inflammatory response and undergoes crosstalk with inflammatory cytokines to exacerbate brain damage following intracerebral haemorrhage in mice. J Neuroinflammation 17(1), 364. doi: 10.1186/s12974-020-02015-9. [PubMed: 33261639]

Wang X, Haroon F, Karray S, Martina D, and Schluter D (2013). Astrocytic Fas ligand expression is required to induce T-cell apoptosis and recovery from experimental autoimmune encephalomyelitis. Eur J Immunol 43(1), 115–124. doi: 10.1002/eji.201242679. [PubMed: 23011975]

Winner B, Jappelli R, Maji SK, Desplats PA, Boyer L, Aigner S, et al. (2011). In vivo demonstration that alpha-synuclein oligomers are toxic. Proc Natl Acad Sci U S A 108(10), 4194–4199. doi: 10.1073/pnas.1100976108. [PubMed: 21325059]

Yang S, Wang J, Brand DD, and Zheng SG (2018). Role of TNF-TNF Receptor 2 Signal in Regulatory T Cells and Its Therapeutic Implications. Front Immunol 9, 784. doi: 10.3389/fimmu.2018.00784. [PubMed: 29725328]

Yanguas-Casas N (2020). Physiological sex differences in microglia and their relavence in neurological disorders Neuroimmunology and Neuroinflammation 7.

Zengeler KE, and Lukens JR (2021). Innate immunity at the crossroads of healthy brain maturation and neurodevelopmental disorders. Nat Rev Immunol 21(7), 454–468. doi: 10.1038/s41577-020-00487-7. [PubMed: 33479477]

Zheng T, and Zhang Z (2021). Activated microglia facilitate the transmission of alpha-synuclein in Parkinson's disease. Neurochem Int 148, 105094. doi: 10.1016/j.neuint.2021.105094. [PubMed: 34097990]

Main Points:

1. Microglial NF-kappaB modulates rotenone-induced pathological progression that is highly sex-dependent.
2. Reduction of neurodegeneration, despite excessive misfolded alpha-synuclein accumulation, link glial inflammation to PD disease outcome.

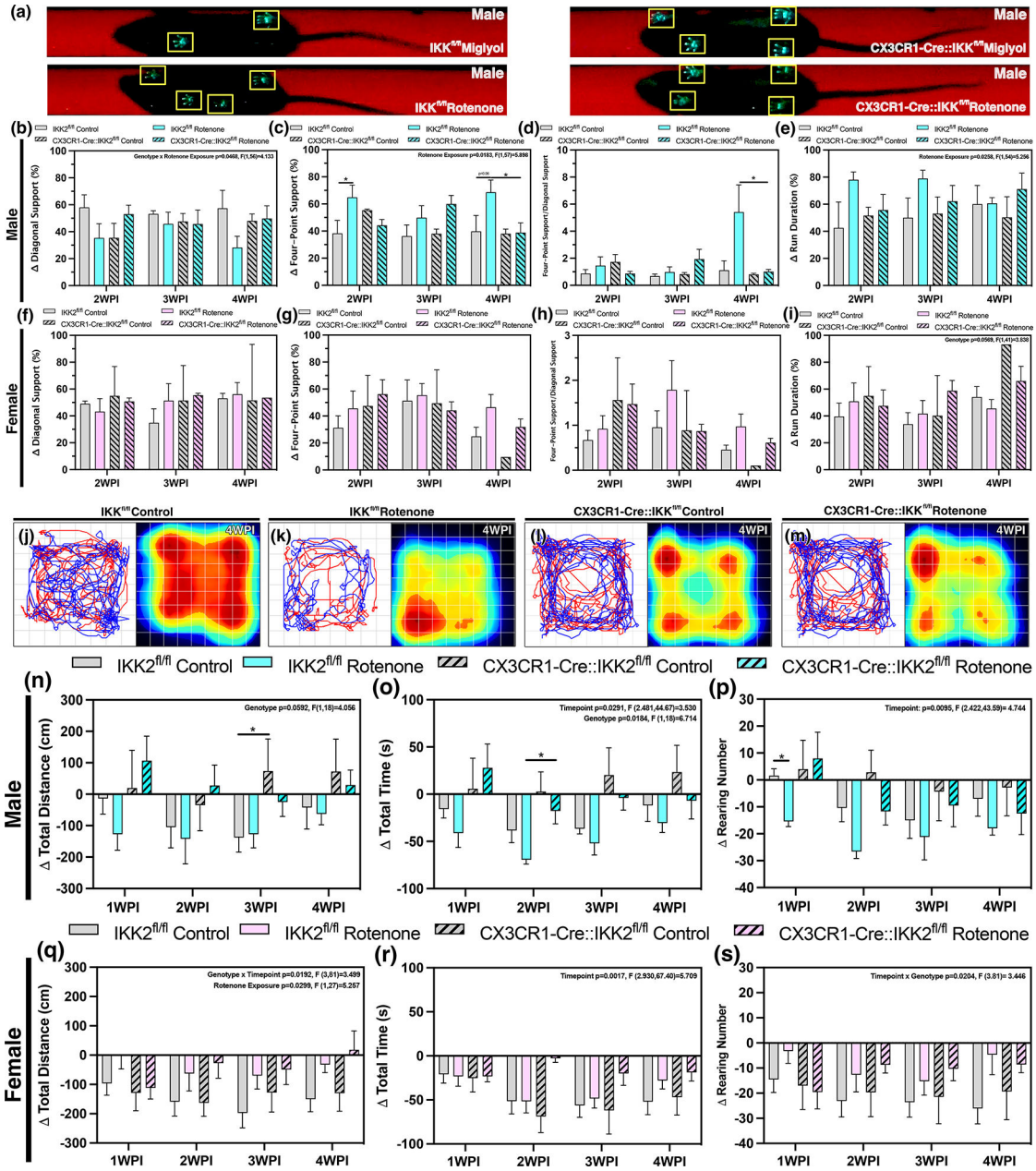

Figure 1. Behavioral analysis of rotenone-exposed mice identifies sex- and genotype-dependent neurological impairments.

(**a**) Specific gait parameters in freely moving animals were analyzed through image processing of digital video captured using a trackway-based system. Neurobehavioral changes in male WT and KO mice were determined for diagonal support (**b**), four-point support (**c**), diagonal support:four point support ratio (**d**), and run duration (**e**). Altered neurobehavioral function in WT and KO female mice was likewise determined for diagonal support (**f**), four-point support (**g**), diagonal support:four point support ratio (**h**), and run duration (**i**). Open field behavioral data are shown as both linear and heatmap representations for male mice in the WT control (**j**), WT rotenone-exposed (**k**), KO control (**l**), and KO rotenone-exposed (**m**) groups. Quantitative analysis of open field data is

presented for male WT and KO mice for change in total distance moved (**n**), total time spent moving (**o**), and rearing number (**p**) recorded during the five-minute analysis window. Data for female WT and KO mice were also analyzed for in total distance moved (**q**), total time spent moving (**r**), and rearing number (**s**). Trackway analysis: n=9 per group. Open field analysis n=6 per group. *p<0.05

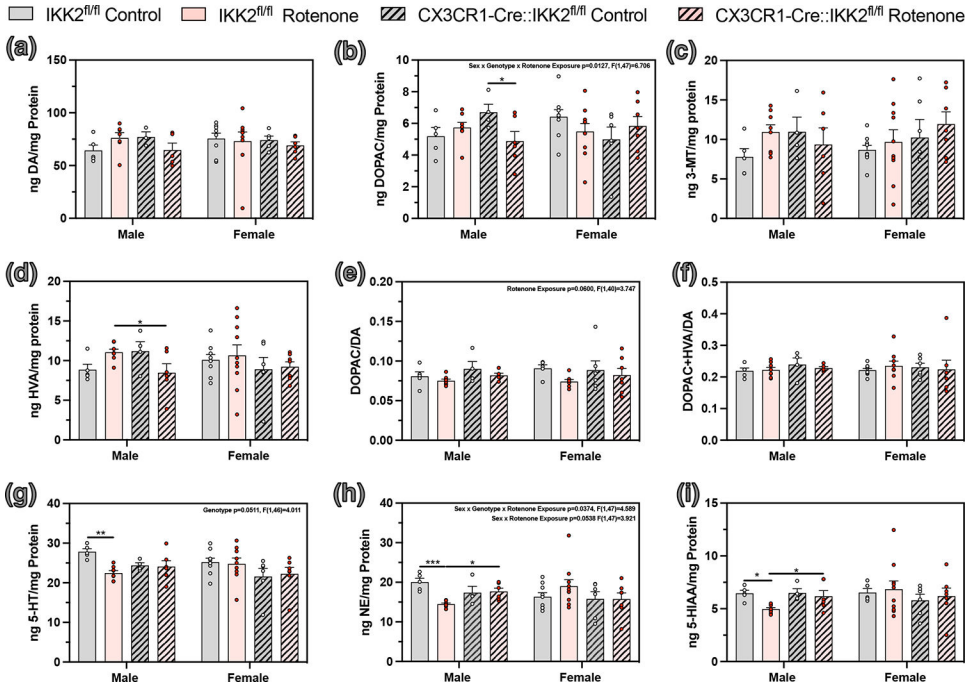

Figure 2. Neurochemical alterations in male animals are rescued in microglia-specific IKK2 knockout mice.

Analysis of catecholamines and monoamines in male and female animals within WT and KO control and rotenone-exposed groups for (**a**) DA, (**b**) DOPAC, (**c**) 3-MT, (**d**) HVA, (**e**) DOPAC:DA ratio and (**f**) DOPAC+HVA:DA ratio, (**g**) 5-HT, (**h**) NE, and (**i**) 5-HIAA. Significant changes in the metabolism of DA and 5-HT were detected only in WT male mice and were prevented by microglia-specific deletion of IKK2. n=9 per group. *p<0.05, **p<0.01, ***p<0.001.

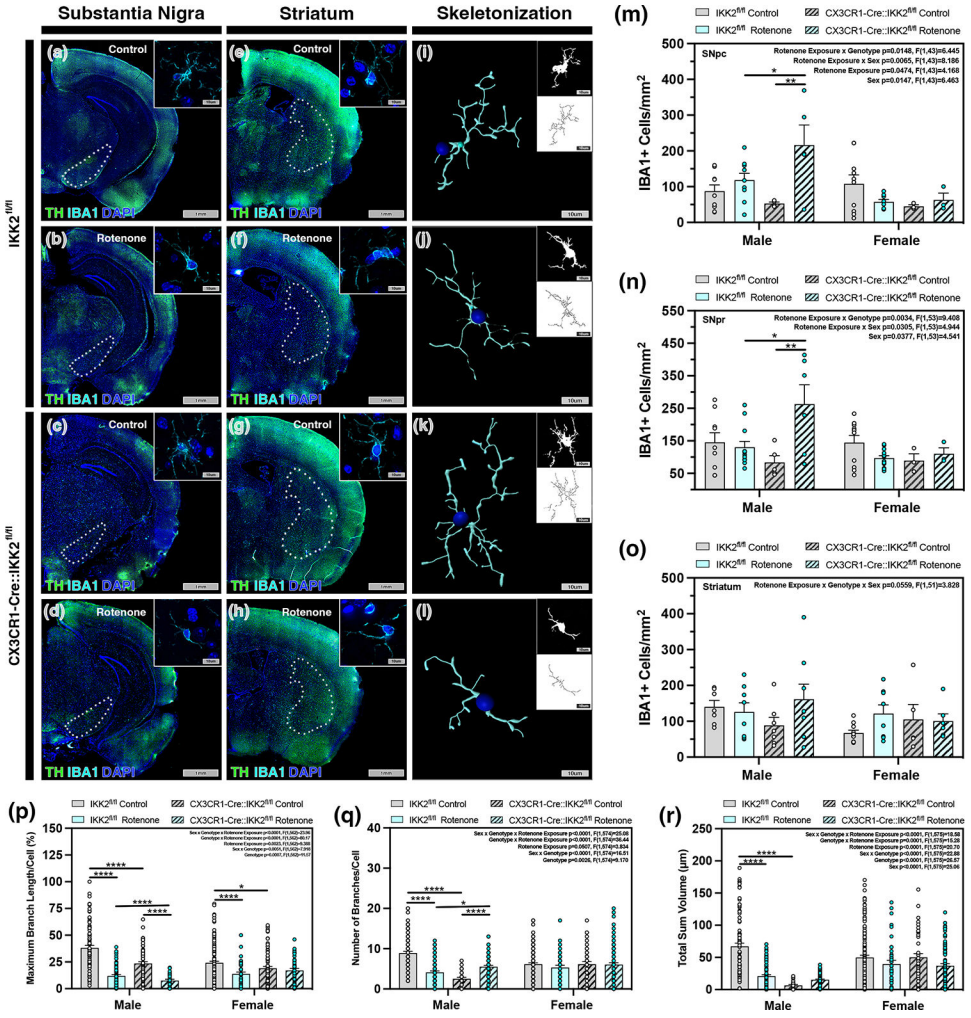

Figure 3. Microglial IKK2 knock-out in male animals exposed to rotenone results in increased microglial recruitment, regional cell density and morphometric indices of activation.

Representative hemispheric 10X montage images from male mice are depicted for the basal midbrain encompassing the SN (**a-d**) and the ST (**e-h**) with immunostaining for microglia (IBA1, cyan) and DAn (TH, green). To analyze microglia morphology, single-cell high magnification images (insets) were collected from the SN and three-dimensional renderings constructed along with binary and skeletonization representations using Imaris Bitplane (**i-l**). Quantification of regional counts of IBA1^{+} cells per area were analyzed for the SNpc (**m**), SNpr (**n**), and ST (**o**). Phenotypic and morphometric discrimination of microglia was determined by analyzing maximal branch length (**p**), branch number per cell (**q**), and branch volume per cell (**r**). n=9 per group. *p<0.05, **p<0.01, ****p<0.0001.

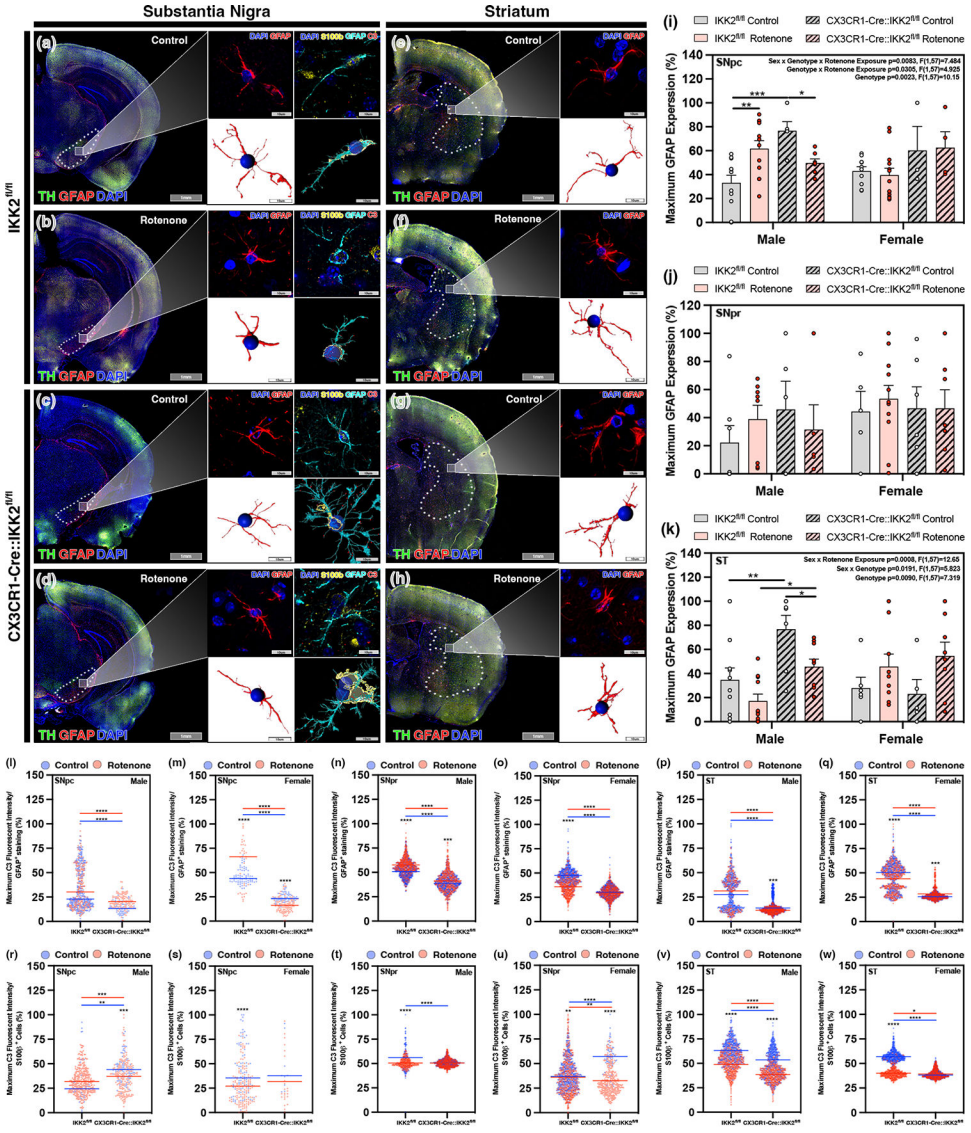

Figure 4. Knockout of IKK2 in microglia selectively reduces populations of reactive astrocytes in male mice exposed to rotenone and decreases expression of complement C3 preferentially in astrocytic processes.

Representative hemispheric 10X montage images from male mice are depicted for the basal midbrain encompassing the SN (**a-d**) and the ST (**e-h**) with immunostaining for astrocytes (GFAP, red) and DAn (TH, green), with 100X high-magnification images and accompanying three-dimensional renderings of reactive astrocytes (GFAP, red, cyan; S100β, yellow; and C3, red). Immunostaining was quantified for each brain region and the maximum expression of GFAP (% per regional area) was analyzed for the SNpc (**i**), SNpr (**j**), and ST (**k**). Maximal C3 expression in $GFAP^+$ processes in male and female mice was determined within the SNpc (**l, m**), SNpr (**n, o**), and ST (**p, q**), respectively. Maximal C3 expression in $S100\beta^+$ soma in male and female mice is shown for the SNpc (**r, s**), SNpr (**t, u**), and ST (**v, w**), respectively. n=9 per group. *p<0.05, **p<0.01, ***p<0.001, ****p < 0.0001.

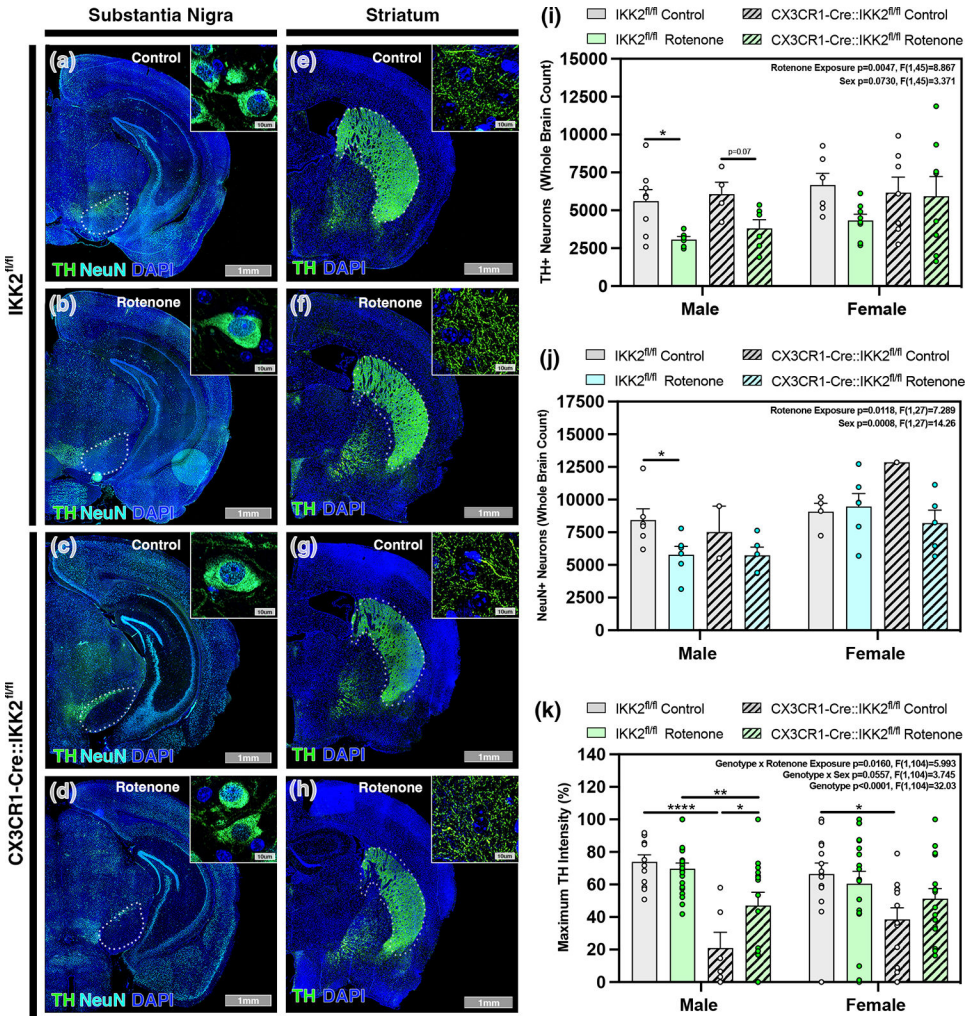

Figure 5. Microglial-specific IKK2 knockout reduces loss of dopaminergic neurons in male animals.

Montage representative hemispheric images of male mice within the basal ganglia are shown for the SN (**a-d**) and ST (**e-h**), with immunostaining for DAn (TH, green) and total neurons (NeuN, cyan), with 100X high-magnification insets. (**i**) Dopaminergic soma were decreased in male WT rotenone-exposed animals, which was prevented in KO males. Pan-neuronal staining shows decreases in overall neuronal soma within the SNpc in male WT rotenone-exposed animals, which was also recovered in KO rotenone-exposed animals (**j**). Intensity measurements for projecting TH^+ dopaminergic fibers in the ST showed decreases in TH intensity in both female and male animals. There were also decreases in TH^+ terminals within male KO rotenone-exposed animals when compared to WT rotenone exposed animals (**k**). n=9 per group. *p<0.05, **p<0.01, ****p < 0.0001.

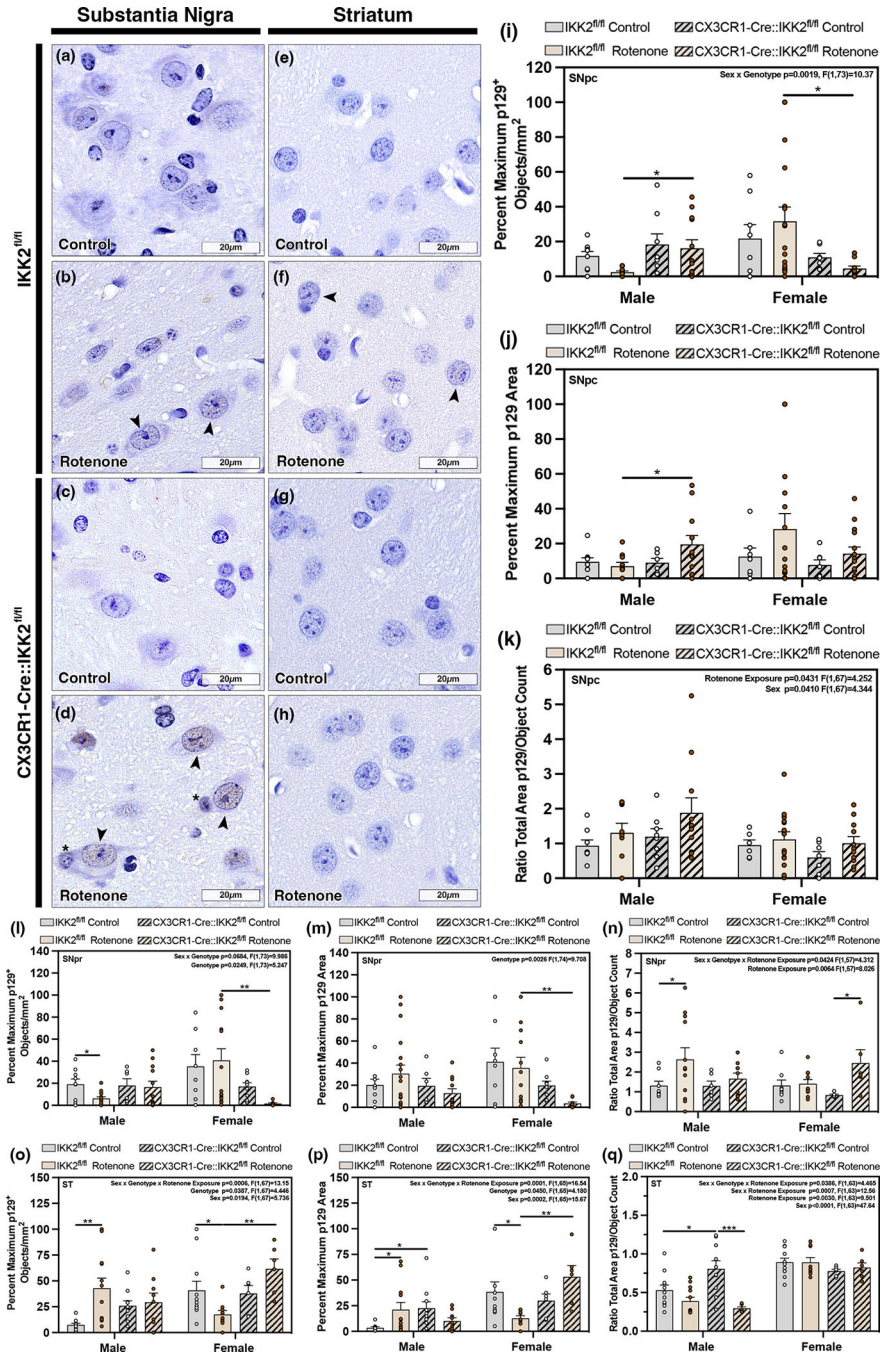

Figure 6. Microglial NF-κB inhibition results in accumulation of misfolded α-synuclein with a distribution that varies by brain region and sex.

Brain sections from each group were labeled by immunohistochemistry for p129 and imaged at high resolution using brightfield scanning microscopy for the SN (**a-d**) and ST (**e-h**). The regional distribution of p129 was quantified by the number of events per area, the maximal $p129^+$ occupied area, and by the ratio of $p129^+$ occupied area to the number of $p129^+$ objects, for the SNpc (**i-k**), SNpr (**l-n**), and ST (**o-q**). n=9 per group. *p<0.05, **p<0.01.

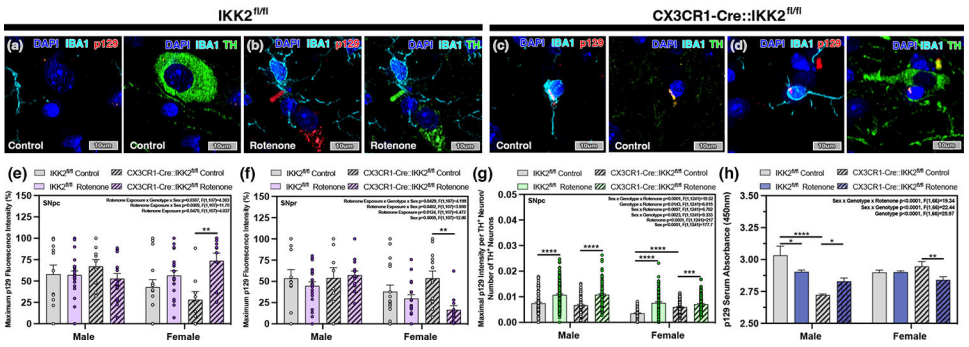

Figure 7. Inhibition of microglial IKK2 increases accumulation of misfolded α-synuclein in dopaminergic neurons.

High magnification 100X images of misfolded α-syn (p129, red), DAn (TH, green), and microglia (IBA1, cyan) in the SN of male WT control (**a**) and WT rotenone-exposed (**b**), and KO control (**c**) and KO rotenone-exposed (**d**) animals. The maximal intensity of $p129^{+}$ events was analyzed by region in the SNpc (**e**) and SNpr (**f**) of male and female animals. (**g**) The maximal $p129^{+}$ intensity in stereologically normalized TH^{+} dopaminergic neuronal soma was quantified in male and female animals. (**h**) Serum p129 was quantified by ELISA (relative absorbance units, A.U.) in serum samples from male and female animals. n=9 per group. *p<0.05, **p<0.01, ****p<0.0001.

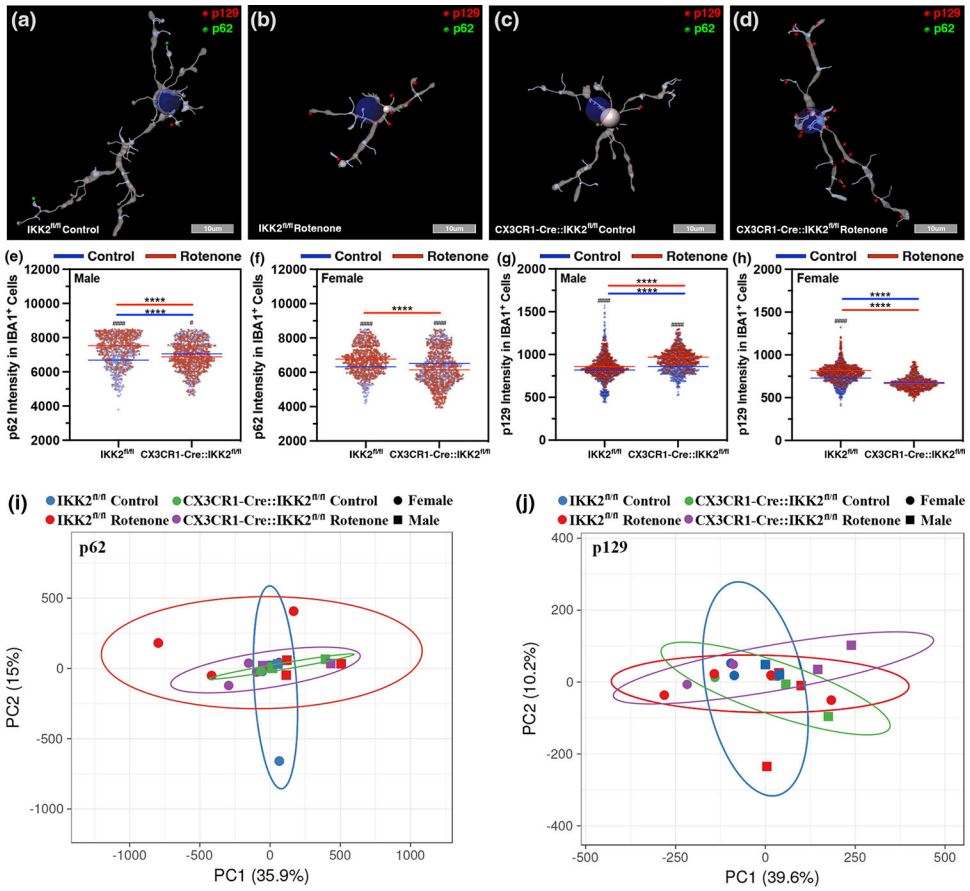

Figure 8. Sequestosome 1 mediated autophagy of p129 is inhibited in IKK2 knock-out animals.

High magnification three-dimensional renderings from multi-immunolabeled sections were acquired from images of individual microglial cells within the SN, depicting areas of $p62^+$ (green) and $p129^+$ (red) events in WT control (**a**), WT rotenone-exposed (**b**), KO control (**c**), and KO rotenone-exposed (**d**) mice. The overall intensity of $p62^+$ immunolabeling was analyzed within individual $IBA1^+$ microglial cells in male (**e**) and female (**f**) animals in control (blue) and rotenone-exposed groups (red). The overall fluorescence intensity of $p129^+$ immunolabeled events in individual $IBA1^+$ cells was analyzed in male (**g**) and female (**h**) animals in control (blue) and rotenone-exposed (red) mice. Principal component analysis of individual exposure groups separated by genotype and sex were analyzed for the presence of $p62^+$ (**i**) and $p129^+$ (**j**) events in the SN of each exposure group. n=9 per group. #p<0.01 intra-genotype comparison, ####p<0.0001 intra-genotype comparison, ****p<0.0001.

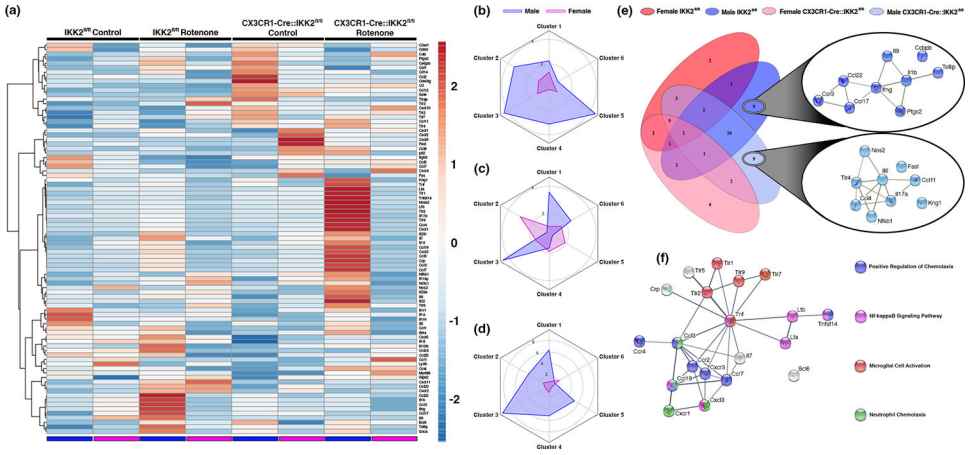

Figure 9. Analysis of differentially expressed genes in the substantia nigra indicates that IKK2 in microglia modulates numerous transcripts associated with innate and adaptive immunity and inflammation following exposure to rotenone.

The extent of differential gene expression in control and rotenone-exposed mice varied with genotype, sex and rotenone exposure, indicating increased levels of invading peripheral immune cells and resulting inflammation in the SN. (**a**) Heat map analysis of the fold-change in expression of differentially regulated inflammatory genes during rotenone-induced neurodegeneration in the SN in WT and KO male (blue sub-indication) and female (pink sub-indication) animals. Radar graph maps of cluster-specific genes were analyzed for male (blue) and female (pink) animals in WT rotenone-exposed (**b**), KO control (**c**) and KO rotenone-exposed (**d**) mice, where the clusters are as follows: 1) Regulation of TLRs by endogenous ligands, 2) neutrophil and monocyte chemotaxis, 3) TNFR2 non-canonical NF-κB pathway activation, 4) astrocyte, monocyte and T-cell chemotaxis, 5) Jak-stat signaling, and 6) complement and coagulation cascades. Venn diagram analysis of all significantly up-regulated genes in rotenone exposed animals (**e**) indicated 9 genes that are discreetly upregulated in male rotenone-exposed mice for both WT and KO groups. STRING mapping of the 20 shared genes upregulated in male rotenone-exposed animals (**f**) revealed genes responsible for positive regulation of chemotaxis (blue), NF-κB signaling (pink), microglial cell activation (red) and neutrophil chemotaxis (green). n=3 per group.

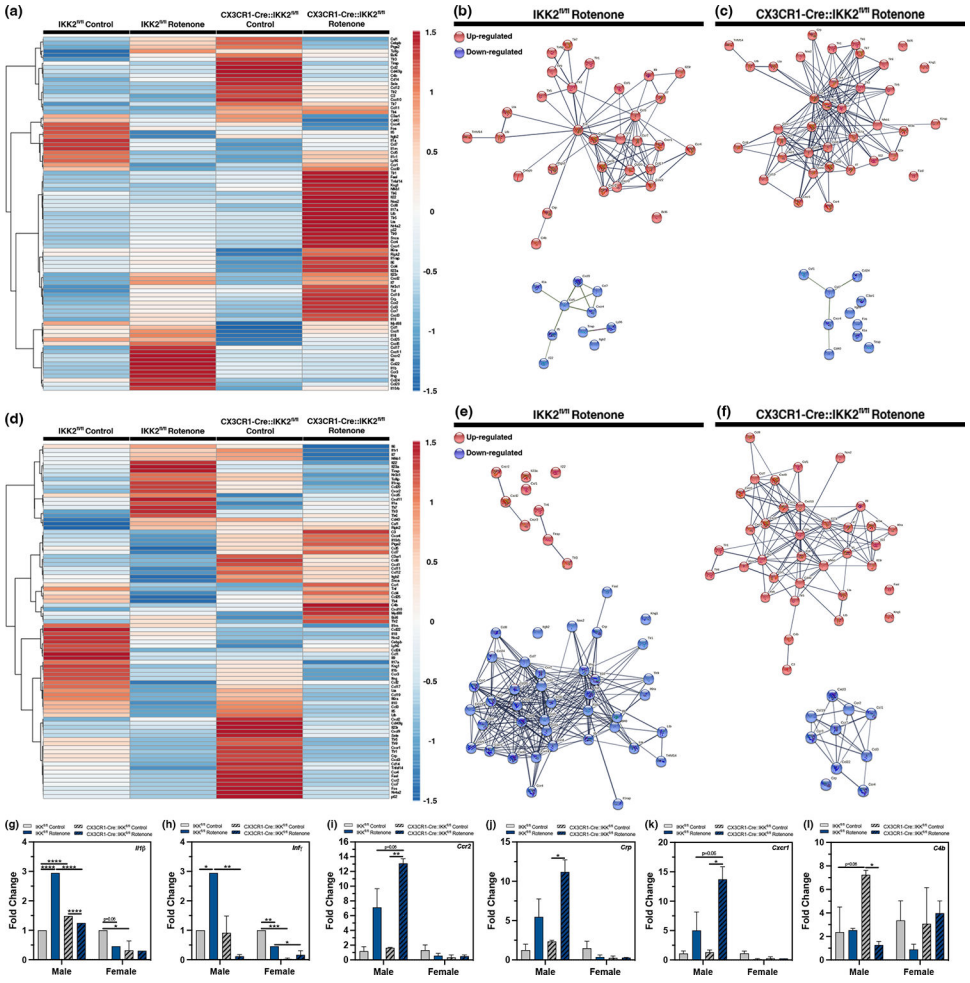

Figure 10. Sex-dependent regulation of inflammatory factors indicates that microglia in male mice mediate cellular recruitment and T-cell interactions.

Heat map analysis of gene expression in male (**a**) and female animals (**d**), respectively. Differentially regulated genes were further analyzed by STRING mapping to compare up-regulated and down-regulated transcripts in male WT (**b**) and KO (**c**) animals. Similarly, STRING mapping was used to compare genes that are up-regulated and down-regulated in female WT (**e**) and KO (**f**) animals. Differential expression of individual transcripts associated with neuroinflammation are depicted for *Il1β* (**g**), *Infγ* (**h**), *Ccr2* (**i**), *Crp* (**j**), and *C4b* (**k**) in male and female animals of each genotype and exposure group. n=3 per group. *p<0.05, **p<0.01, ***p<0.001, ****p < 0.0001.